Mercury stocks in discontinuous permafrost and their mobilization by river migration in the Yukon River Basin

M. Isabel Smith[1*], Yutian Ke[2], Emily C. Geyman[2], Jocelyn N. Reahl[2], Madison M. Douglas[2,4], Emily A. Seelen[1], John S. Magyar[2], Kieran B.J. Dunne[2,5], Edda A. Mutter[3], Woodward W. Fischer[2], Michael P. Lamb[2], A. Joshua West[1]

1. Department of Earth Sciences, University of Southern California, Los Angeles, CA 90089, USA
2. Division of Geological and Planetary Sciences, California Institute of Technology, Pasadena, CA 91125, USA
3. Yukon River Inter-Tribal Watershed Council, Anchorage, AK 99501, USA
4. Department of Earth, Atmospheric, and Planetary Sciences, Massachusetts Institute of Technology, Cambridge, MA 02139, USA
5. Delft University of Technology, 2628 CD Delft, Netherlands

*Corresponding author email: smithmi@usc.edu

Abstract: Rapid warming in the Arctic threatens to destabilize mercury (Hg) deposits contained within soils in permafrost regions. Yet current estimates of the amount of Hg in permafrost vary by ~4 times. Moreover, how Hg will be released to the environment as permafrost thaws remains poorly known, despite threats to water quality, human health, and the environment. Here we present new measurements of total mercury (THg) contents in discontinuous permafrost in the Yukon River Basin in Alaska. We collected riverbank and floodplain sediments from exposed banks and bars near the villages of Huslia and Beaver. Median THg contents were $49^{+13}/_{-21}$ ng THg g sediment^{-1} and $39\ ^{+16}/_{-18}$ ng THg g sediment^{-1} for Huslia and Beaver, respectively (uncertainties as 15th and 85th percentiles). Corresponding THg:organic carbon ratios were $5.4^{+2}/_{-2.4}$ Gg THg Pg C^{-1} and $4.2\ ^{+2.4}/_{-2.9}$ Gg THg Pg C^{-1}. To constrain floodplain THg stocks, we combined measured THg contents with floodplain stratigraphy. Trends of THg increasing with smaller sediment size and calculated stocks in the upper 1 m and 3 m are similar to those suggested for this region by prior pan-Arctic studies. We combined THg stocks and river migration rates derived from remote sensing to estimate particulate THg erosional and depositional fluxes as river channels migrate across the floodplain. Results show similar fluxes within uncertainty into the river from erosion at both sites ($95\ ^{+12}/_{-47}$ kg THg yr^{-1} and $26\ ^{+154}/_{-13}$ kg THg yr^{-1} at Huslia and Beaver, respectively), but different fluxes out of the river via deposition in aggrading bars ($60\ ^{+40}/_{-29}$ kg THg yr^{-1} and $10^{+5.3}/_{-1.7}$ kg THg yr^{-1}). Thus, a significant amount of THg is liberated from permafrost during bank erosion, while a variable but generally lesser portion is subsequently redeposited by migrating rivers.

Keywords: Mercury, Arctic, Permafrost, Erosion, Rivers

Introduction:

The Arctic is warming four times [1] faster than the global average, destabilizing permafrost soils that have remained frozen for two or more years that underlie much of the Arctic [2,3]. While moderate climate scenarios project 15%-87% permafrost loss by 2100, extreme scenarios estimate up to 99% loss [4–6]. Permafrost loss poses multiple threats to the estimated 5 million people who live in the Arctic, with 3.3 million people living in areas where permafrost is predicted to degrade and disappear by 2050 [7]. Thawing permafrost can damage critical infrastructure [8,9], impact navigable routes [10], and decrease food security, particularly for communities with subsistence practices [10,11]. Additionally, permafrost thaw may release contaminants that have been locked away in frozen soils for millennia [12]. The potential release of large amounts of mercury (Hg) from permafrost has received particular attention due to its threat to human health [12,13].

Due to atmospheric circulation [14] and preservation of organics in frozen soils [9,10], permafrost Hg has accumulated over thousands of years, and Hg in the top meter of Arctic soils potentially exceeds the total amount stored in the atmosphere, ocean, and all other soils [15–17]. However, estimates of the amount of total mercury (THg) stored in permafrost soils are poorly constrained, ranging from 184 to 755 Gg THg [15–17]. Varying estimates stem from under-sampling of Arctic soils, forcing studies to rely on sparse field data and models to determine THg stocks. Mercury to organic carbon ratios (RHgC) are often used for extrapolation due to relatively more abundant carbon data availability and first-order correlation between Hg and carbon in many settings. However, RHgC are in fact highly variable ($\tilde{x}$=2.0±1.9, [15]) and need to be better constrained for their use as a Hg proxy across Arctic soil types. Additionally, existing THg stock measurements are limited to the top 3 meters, primarily due to practical limitations of soil coring, even though deeper sediments may be important stores of Hg and other constituents [18].

Quantifying Hg stocks and understanding its remobilization to biologically active zones is important as liberation of this Hg during permafrost thaw could be detrimental to Arctic communities. A proportion of mobilized inorganic Hg (~1% in the Yukon River Basin (YRB)) is bacterially transformed into methylmercury [19], a neurotoxin that bioaccumulates in organisms affecting animal and human health when consumed [20–24]. Many Indigenous communities, including Alaska Native communities, rely on subsistence fishing and have disproportionately elevated blood Hg levels linked to dietary exposure [25, 26]. Altering Hg inputs to Arctic waterways has an immediate and direct impact on Hg exposure in these communities, as well as affecting the Hg delivered to ecosystems and the Arctic Ocean.

Despite its potentially deleterious effects, the amount of Hg in permafrost and its mobility during thaw are not well understood. While a range of processes can release Hg from permafrost, including gaseous evasion [27], aqueous leaching [13,19], and particulate erosion [15], river erosion can also contribute substantially by quickly mobilizing large amounts of sediment [17,28,29]. To better constrain floodplain THg stocks and quantify release from erosion of permafrost deposits, we present a new dataset of THg measurements in riverbank and floodplain

sediments. We also employ a mass balance approach to evaluate the role of net river migration on erosional and depositional THg sediment fluxes in the YRB of Alaska.

Methods

Sampling Sites

The YRB spans more than 330,000 km^2 in regions of northwestern Canada and central Alaska and is underlain by areas of continuous and discontinuous permafrost [30]. The Yukon River has the highest flow-weighted annual THg concentration out of the six major Arctic rivers [29] and the YRB is one of the six major freshwater contributors to the Arctic Ocean, supplying 3-32 times more THg to the oceans than the 8 other major northern hemisphere river basins [19]. This makes the YRB an important focus of study in the context of riverine THg inputs in a changing Arctic.

Yukon river waters contain a range of sediment sizes, which are expected to influence organic carbon (OC) and Hg contents. To capture some of this variability, we focused on two regions in the YRB underlain by discontinuous permafrost with distinct riverbed sediment characteristics (**Figure 1**). Our sites were chosen near Alaska Native communities that are at different risk levels for erosion, flooding, and permafrost thaw [31,32] to coincide with overarching collaborative efforts to understand the effects of erosion in the YRB. At both sites, the river channel migrates laterally through cutbank erosion and point bar deposition at rates of meters per year [33].

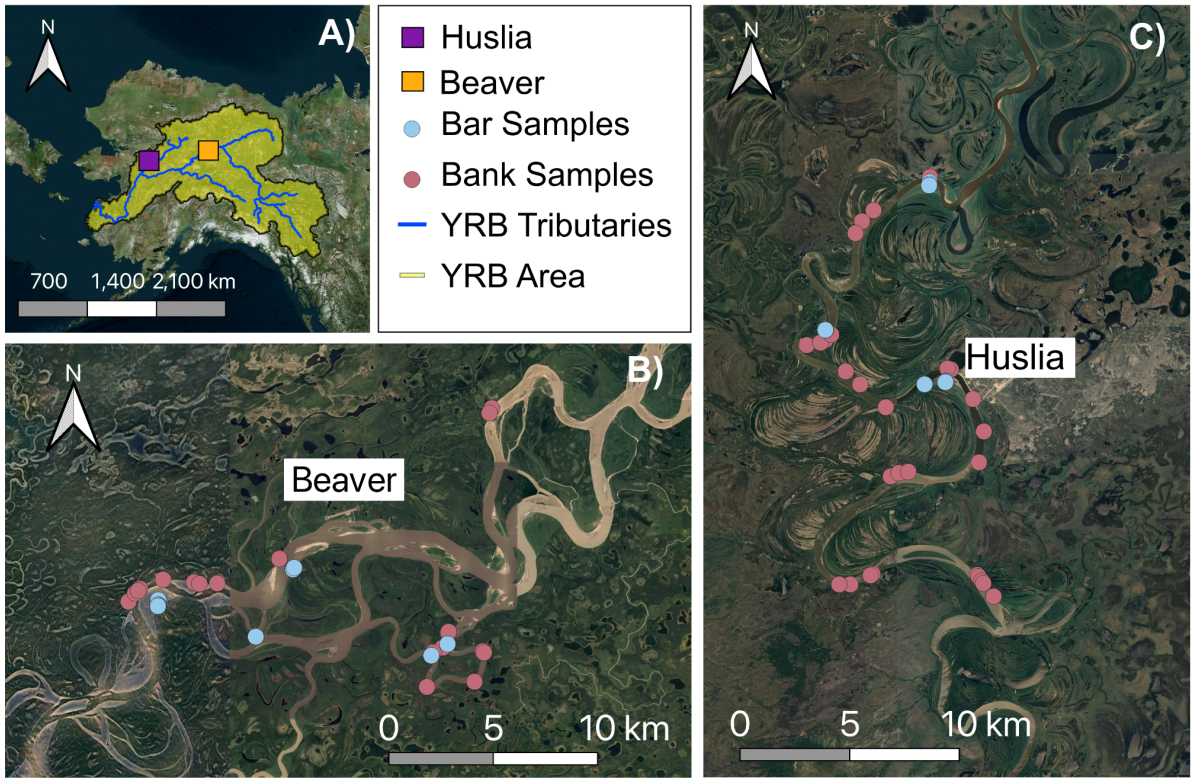

Figure 1: Study sites located in interior Alaska in the YRB (watershed boundary-yellow shaded

region [34], tributaries-blue line) (**A**). Samples were collected along an anastomosing, gravel-bedded reach of Yukon River **(B)** and a sand-bedded reach of the Koyukuk River **(C)**, a single-threaded meandering river that is a major tributary of the Yukon River. Sampling locations were located near the villages of Huslia (purple square in A) and Beaver (orange square). Dots represent cutbanks (red; n = 56) and point bars (blue; n = 29) that have been characterized. Samples were collected in June 2022 (Huslia: 18 cutbanks, 6 point bars; Beaver: 13 cutbanks, 6 point bars) and September 2022 (Huslia: 15 cutbanks, 8 point bars; Beaver: 10 cutbanks, 6 point bars) (**Supplementary**, **Dataset S1**). To capture a holistic view of the floodplain, sites were selected to span a range in ages, terrain type, and permafrost presence determined from geomorphic maps [33,35,36]. Seasonal variation in water level affected sampling site accessibility, so sites from June and September are complimentary, but not identical. Basemaps: Bing Maps (Earthstar Geographics LLC SIO) and Google Earth (Maxar Technologies) [37,38]. Yukon River Watershed Boundary shapefile reproduced with permission from [34] with permission from the Yukon River Inter-Tribal Watershed Council.

Field Sampling Procedures

Sediment samples were collected from exposed riverbanks and pits dug (~0.5-1 m deep) into point bar deposits (**Figure 1B, 1C, Supplementary, Text S1**). Stratigraphic columns were measured from the top of the bank to the waterline or from the top of the pit to the bottom of the pit, which was usually frozen ground. Descriptions of stratigraphic columns, distinct bed thickness, sample depth, and substrate class (gravel, sand, peat, mud) were recorded. The surficial 5-10 cm of exposed sediments were removed before sample collection. Paired samples were collected for analysis of geochemistry and bulk density (details in **Supplement, Text S1**). At selected permafrost cutbanks, we sampled both thawed material on the surface (effectively the "active layer" of material exposed on the vertical bank) and frozen material recovered by drilling into the bank with a hole saw.

Lab Analysis

Sediment samples for geochemical analysis were freeze dried and split. Geochemical subsamples were ground into a homogeneous fine powder in an agate mortar and pestle (**Supplementary, Text S2**). THg contents were determined using a NIC direct mercury analyzer (MA-3000) at the University of Southern California using the United States Geological Survey Mercury Research Laboratory protocol [39,40]. Analysis of reference material MESS-4 (90 ± 40 ng/g, National Research Council Canada) showed a median value of 64.9 ± 2.6 ng Hg g^{-1} (**Supplementary, Figure S1**, with uncertainty reported as relative standard deviation, or RSD) and blanks were below detection. All sediment samples were run in multiples (100% duplicate, 18% triplicate; median RSD of 2.03% (**Supplementary, Figure S1, S2**).

Total organic carbon (TOC) content was analyzed using an Elementar elemental analyzer at Woods Hole Oceanographic Institute's National Ocean Sciences Accelerator Mass Spectrometry Facility (NOSAMS, [41]). 38% of samples were analyzed in duplicate, yielding a

median RSD of 5%. The analytical precision was assumed to be less than 1%. TOC (wt%) and THg content were used to calculate RHgC, reported as μg Hg g C^{-1} [40,41]. Bulk density samples were weighed pre- and post-oven drying (80°C) to determine water mass fraction and dry density. Samples were categorized visually using a grain-size card into substrate classes of sand, mud, peat, and gravel. For each field site, THg content and RHgC values were sorted by substrate composition and a one-way ANOVA test ($\alpha < 0.05$) was conducted to determine if substrate compositions were statistically different from each other.

Stock Calculations

We calculated THg stocks for the most complete stratigraphic sections sampled (Huslia: 15 cutbanks and 11 bars; Beaver: 13 cutbanks and 16 bars, **Supplementary, Table S1**). Near-surface stocks were determined by integrating over 1 meter and 3 meters depth to compare with previously published datasets [15–17]. Total stocks that can potentially be reworked by river lateral migration were determined for the full column depth (~10-15 meters), defined as the distance from the top of the cutbank (CB) or point bar (PB) to the bottom of the thalweg (the deepest part of the river). However, incomplete bank exposure and inability to dig below the thawed active layer meant we could not sample below the top ~20-50% of this sedimentary column. Thus, we estimated full column stocks for PB and CB by the sum of the sampled and inferred stocks for each stratigraphic layer in the column (i) (**Equation 1**, **Supplementary, Table S1**).

$$S_{PB\ or\ CB} = \sum_{i=1}^{n} \rho_{dry,i} * h_i * THg_i \quad (1)$$

For exposed sections of bank and bars, sampled stocks were directly calculated using measured layer thicknesses (h_i, km) from each identifiably stratigraphic layer, dry density of bank material (ρ_{dry}, kg dry sediment km^{-3}) and THg mass fraction (THg_i , kg Hg kg dry $sediment^{-1}$) from collected paired samples. Any missing stratigraphic information was supplemented with an average value from sediments of similar substrate composition from the same field location **(Supplementary, Table S2, S3**).

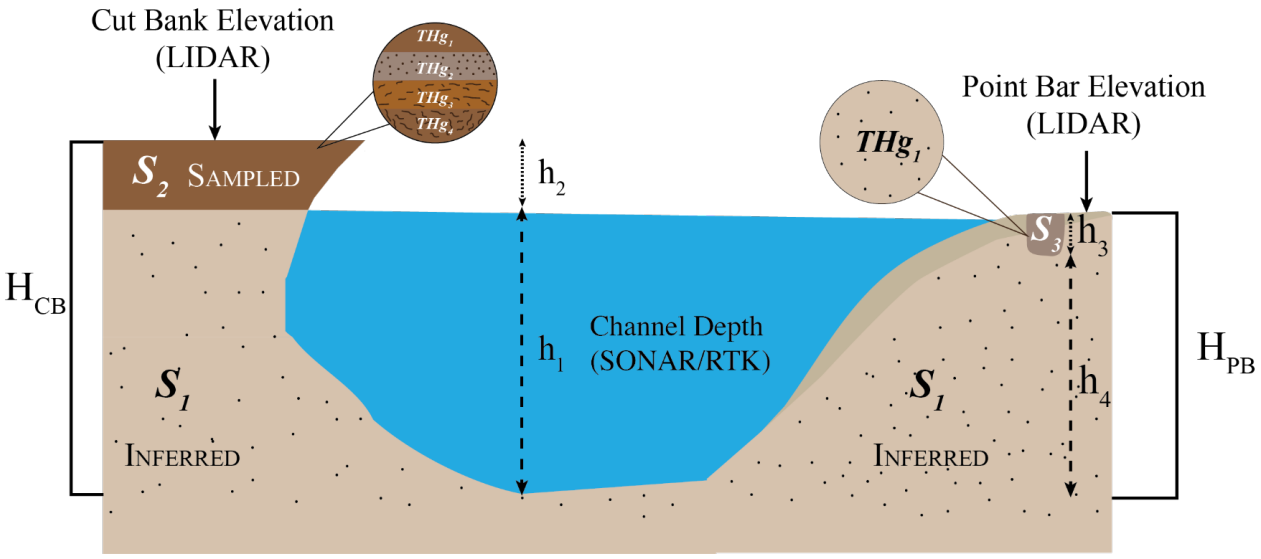

Figure 2: Schematic showing different components of the THg stock (*S*) calculation and where the data for each variable was obtained. Sampled sections were directly measured in the field, while inferred sections were determined using average values based on substrate composition (**Supplementary, Table S1, S4)**. S_2 represents the sampled cutbank stock, with h_2 the corresponding exposed height. S_3 represents the sampled point bar stock, accessed by digging a pit, with h_3 representing associated depth.

To calculate THg stocks for the unsampled sections (the "inferred" portion in **Figure 2**), we determined unsampled column heights and inferred associated sediment properties. Total column heights, independent of river stage height, were determined based on bathymetric and elevation data (**Supplementary, Table S1**). Bathymetry was mapped via SONAR surveys at the time of sample collection, referenced by RTK-GPS (real-time kinematic geographic positioning system). Topography data were from National Center for Airborne Laser Mapping (NCALM) Light Detection and Ranging (LIDAR) datasets from flights over Huslia on August 21-23, 2022, and over Beaver on August 2-5, 2021 (**Figure 2**). The sampled sections (h_2, h_3) were subtracted from total column height (H_{CB}, H_{PB}) to determine the unmeasured sections (h_1, h_4) heights.

To infer sediment properties, we used our most complete stratigraphic sections (~5-10 meters thick), measured in late fall when the Koyukuk (Huslia) and Yukon (Beaver) Rivers were at low stage. We determined that 3 m was a characteristic maximum thickness for fine-grained overbank sediments at both sites (**Supplementary, Figure S3**). We then bootstrap resampled all measured beds below 3 meters depth from the modern floodplain surface to estimate sediment properties of all unmeasured beds. We found that lower beds (> 3m) were predominantly sand in Huslia and a mixture of gravel and sand in Beaver (**Supplementary, Figure S4**). Our findings of grain size fining upward is typical of river lateral accretion deposits [42]. We calculated inferred section stocks using an average dry density and THg content (**Supplementary, Table S4**) based on substrate composition for each location.

Flux Calculations

To calculate the flux of sediment-bound THg going into and out of the river, we created a one-dimensional mass balance box model (**Supplementary**, **Figure S5**) representative of erosion and deposition along our study reaches within the Koyukuk and Yukon Rivers following prior work on OC [43] in the same region. For our most complete stratigraphic sections, we calculated THg fluxes for individual banks and bars (**Supplementary Table S5)** following**:**

$$F = L * k * S_x \text{ where } x = CB, PB \quad (2)$$

Cutbank erosion and point bar deposition flux (F, $kg\ Hg\ y^{-1}$) for Huslia and Beaver were calculated using site-specific river migration rates (k, km y^{-1}) calculated from 10 m resolution Sentinel-2 satellite imagery over the period 2016-2022 [44], THg stocks (S_x, kg Hg km^{-2}), and river reach lengths (L, km) of the entire study areas. Huslia had river reach length of 58 km with migration rates ranging from 0.63-7.6 m y^{-1}, while Beaver had migration rates of 0.10-12 m y^{-1} along the 55 km river reach (**Supplementary, Figure S6, Table S4, S5,** [44]). Uncertainties were estimated via a bootstrapping resampling simulation (n = 10000), selecting random calculated bank and bar fluxes to calculate a median net mercury flux; uncertainties are reported as 15th and 85th percentiles of the resulting distributions. The net flux (F_{net}) from river migration was calculated based on the difference between cutbank (F_{CB}) and point bar (F_{PB}) fluxes, as:

$$F_{net} = -F_{CB} + F_{PB} \quad (3)$$

This approach only quantifies loss or gain of Hg from a river reach due to floodplain erosion and deposition; it does not consider sediment imported from upstream and exported downstream, and as such does not capture all processes mobilizing Hg across the watershed.

Results:

Sediment THg content and RHgC

The median THg content was $49^{+13}/_{-21}$ ng Hg g sediment^{-1} and $39^{+16}/_{-18}$ ng Hg g sediment^{-1} (**Figure 3**, uncertainties reported as 15th and 85th percentiles) for Huslia and Beaver, respectively. The median RHgC for Huslia was $5.4^{+2}/_{-2.4}$ µg Hg g^{-1} C and $4.2^{+2.4}/_{-2.9}$ µg Hg g C^{-1} for Beaver (**Figure 3**). Where we collected paired samples of thawed and frozen material from cutbanks, THg contents were generally lower in the frozen material in Huslia and Beaver had no apparent trends (**Table S6**). We cannot rule out contamination from the hole saw used to sample frozen material as contributing to these differences, but effort was made to remove material that had come into contact with metal during sample collection.

Across all of the samples analyzed, THg content showed no apparent trends with depth (**Figure S7**) and a positive relationship to TOC (**Figure 4 A, D)** and substrate class (p-values < 0.0001, **Figure 4 B, E**). RHgC showed a negative relation to TOC (**Figure S8 C, F)** and

substrate class (p-values < 0.0001, **Figure 4 C, F)**. These results suggest that THg contents in these systems are strongly correlated to substrate class and OC content.

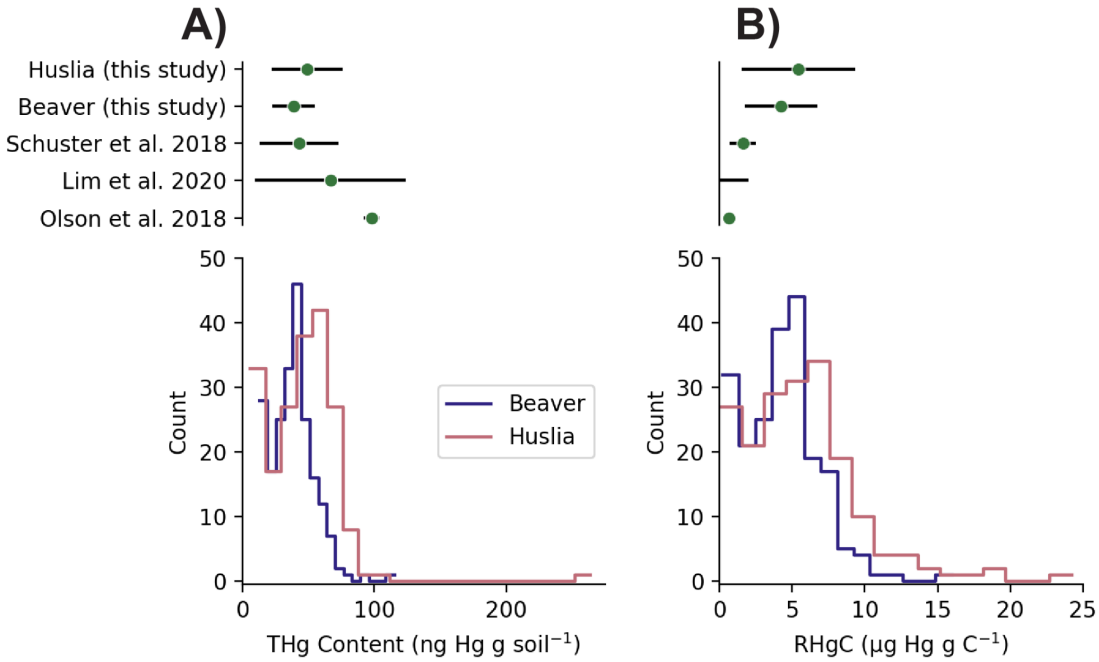

Figure 3: Median (**A**) THg and (**B**) RHgC values from this study and similar pan-Arctic studies (Alaska: Schuster and Olson; Siberia: Lim), with histograms from this study for comparison. Green dots represent the median value and black error bars show the uncertainty in the median from each study. Sample range is given for Lim et al. 2020, as no median was reported.

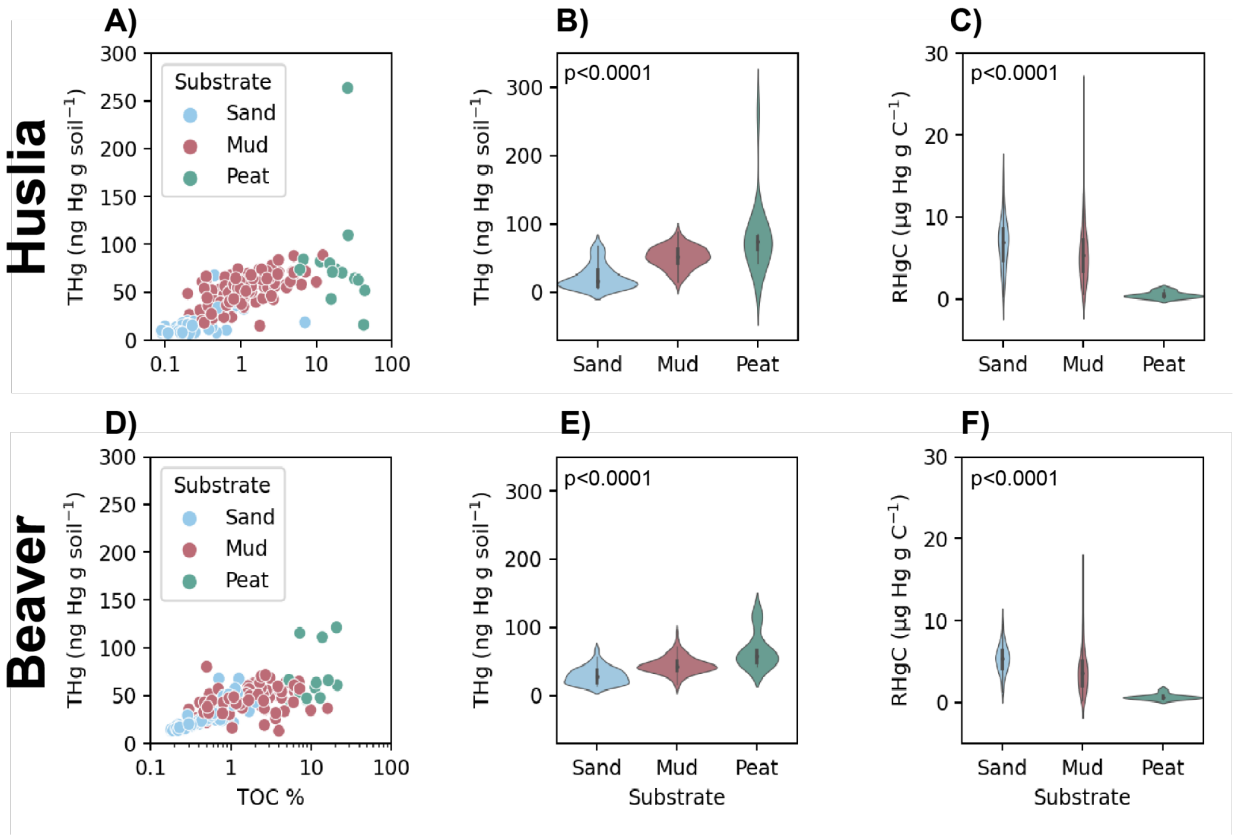

Figure 4: Comparison of THg to TOC% (**A, D**) and substrate composition to THg contents (**B, E**) and RHgC (**C, F**) for Huslia and Beaver. Plots show all 413 samples collected in June and September 2022. THg and RHgC in relation to substrate classes all had $p < 0.0001$.

Hg Stocks and Fluxes

The median heights of the complete stratigraphy from banktop to the channel thalweg at Huslia were 11 m for cutbanks and 10 m for point bars; depths at Beaver were 12 and 11 m, respectively. Median cutbank stocks at Huslia were 41 $^{+6}/_{-20}$, 125$^{+44}/_{-62}$, and 327$^{+123}/_{-39}$ kg Hg km sediment^{-2}, over 1 m, 3 m, and total depths, respectively (**Figure 5**). Equivalent point bar THg stocks at Huslia were 33$^{+4}/_{-11}$, 90$^{+4}/_{-11}$, and 250$^{+7}/_{-63}$ kg Hg km sediment^{-2}. At Beaver, cutbank stocks were 36$^{+13}/_{-8}$, 103$^{+28}/_{-18}$, and 337$^{+44}/_{-76}$ kg Hg km^{-2}, while point bar stocks were 29$^{+6}/_{-4}$, 92$^{+4}/_{-6}$, and 274$^{+37}/_{-85}$ kg Hg km sediment^{-2}. Point bar and cutbank stocks at both Huslia and Beaver overlapped within uncertainty for all depth intervals (**Figure 5)**. The bimodal distribution of THg stocks observed in **Figures 6C, 6D, and 6E** are due to the point bar elevation differences between sites.

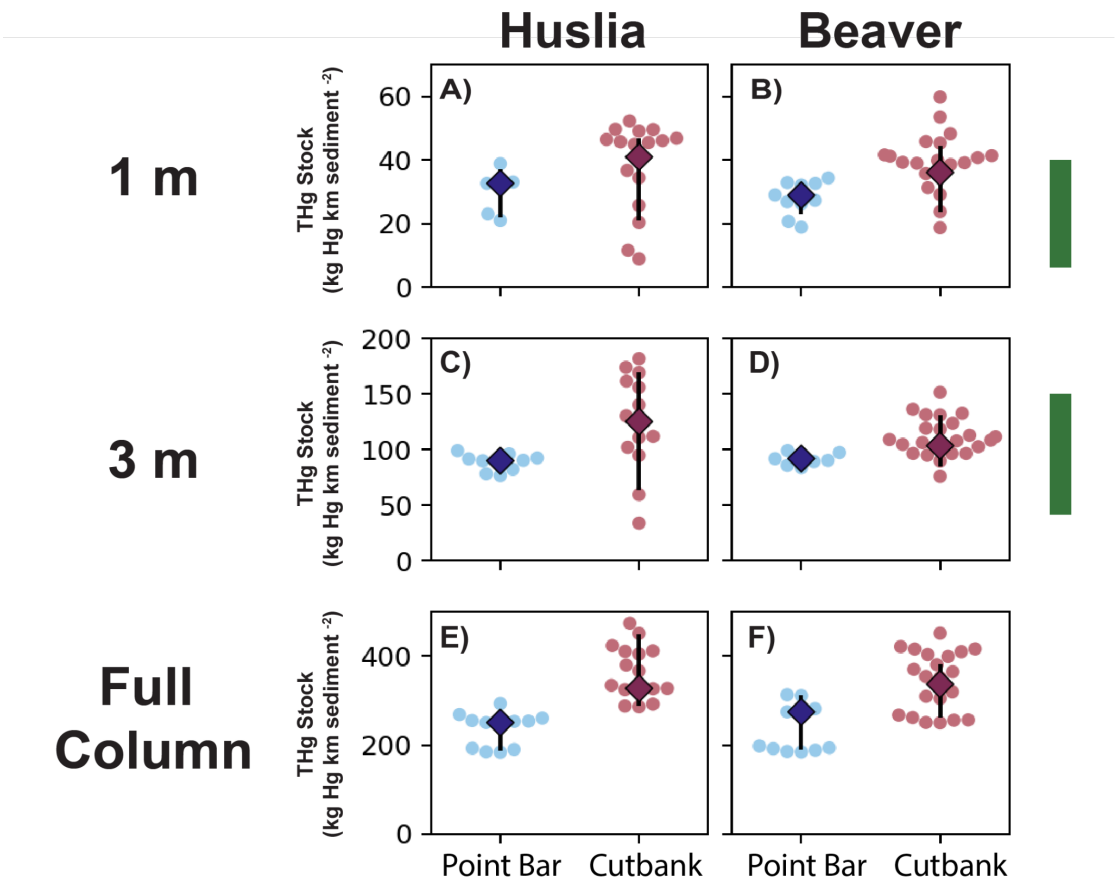

Figure 5: Estimates of THg stocks at depth intervals of 1 m (**A, B**), 3 m (**C, D**), and bank full depth (**E, F**) for Huslia and Beaver. Dots represent individual banks (Beaver: n =13, Huslia: n = 15) or point bars (Beaver: n =16, Huslia: n = 11), while diamonds represent the median of all banks or bars. Error bars represent the 15th and 85th percentiles. Stocks from columns with >30% unmeasured layers or frozen layer stocks were excluded from figure (**Supplement Table S1, Figure S7**). Green bars represent the THg stock (top 1 m: 6-40 kg Hg km sediment^{-2}, top 3 m: 41-150 kg Hg km sediment^{-2}) inferred for the study region from the global maps of permafrost THg reported [15].

The median fluxes at Huslia were 95 $^{+12}/_{-47}$ and 60 $^{+40}/_{-29}$ kg Hg yr^{-1} for cutbank erosion and point bar deposition, respectively. Beaver had corresponding median fluxes of 26 $^{+154}/_{-13}$ and $10^{+5.3}/_{-1.7}$ kg Hg yr^{-1}. The net THg budget associated with river migration for Huslia (+32 $^{+28}/_{-29}$ kg Hg yr^{-1}, reflecting net deposition of THg in point bars) and Beaver (-17$^{+9}/_{-7}$, reflecting net erosion of THg into the river) were calculated as the difference between the median erosion and deposition fluxes, with uncertainties estimated by bootstrap resampling with replacement. Overall, both sites showed similar fluxes of THg release by cutbank erosion, overlapping within uncertainty. However, the THg flux from point bar deposition is significantly higher at Huslia than at Beaver, leading to different estimates of the net budgets.

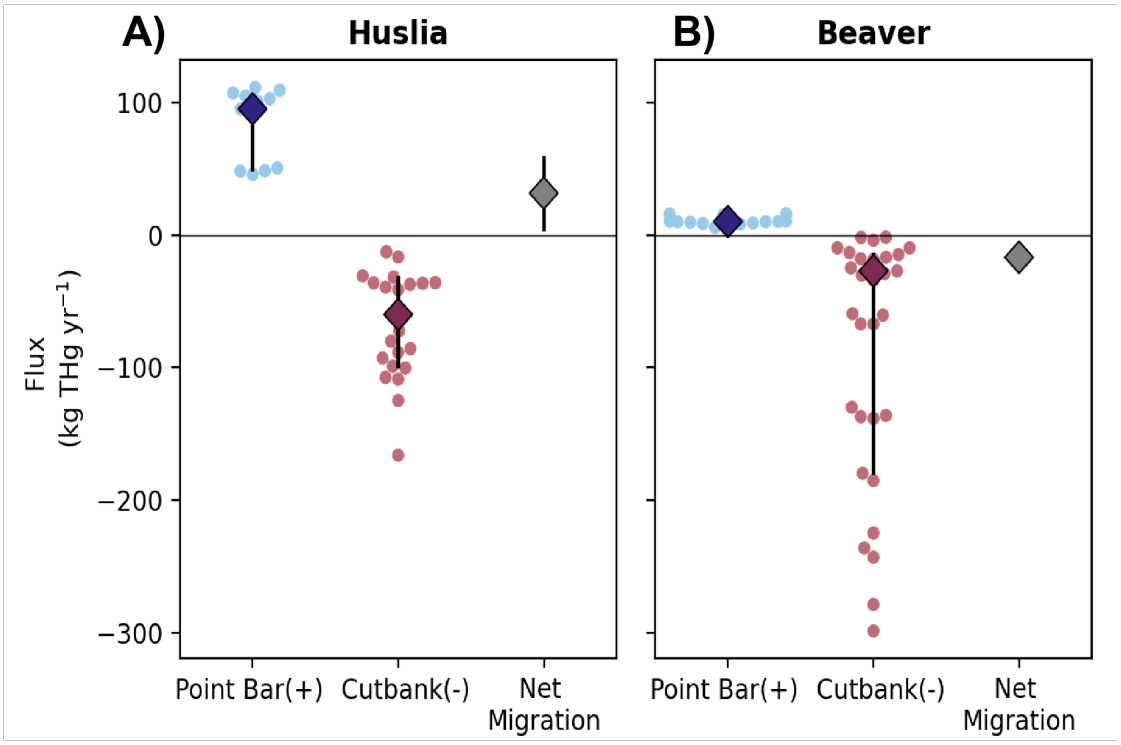

Figure 6: Mercury fluxes from the river to the floodplain (positive direction) due to point bar deposition and cutbank erosion, and the net effect of river migration, for Huslia (**A**) and Beaver (**B**). Dots represent individual calculated bank and bar fluxes while diamonds represent median fluxes. Error bars for point bars and cutbanks are the 15th and 85th percentiles. Error bars for net migration were calculated using a bootstrap resampling method (n=10,000).

Discussion:

Stocks

This study presents new THg and RHgC measurements (**Supplemental Dataset 1**) from the YRB using a spatially dense sampling approach that allows us to determine regional THg stocks with accuracy not possible with prior, more generalized approaches. Median THg values for Huslia and Beaver are similar to those reported in prior studies from Alaska as well as other settings in the Arctic ([15–17]; **Figure 3**).

THg stocks for the upper 3 meters are similar to those predicted for our study region in the map produced by Schuster et al. 2018, who used OC datasets and the RHgC to determine Pan-Arctic THg stocks ([15], **Figure 5**). The consistency of our stock calculations with their predictions may be unsurprising since their model was based on samples collected from interior Alaska. However, our RHgC values were higher than reported in their study and other Arctic studies **(Figure 3**, [15–17]), primarily because of lower OC at our sites. Interestingly, lower carbon content is not reflected in lower THg content in these sediments despite the expected association of Hg and OC. The end result of similar stock values emerges by the coincidence of higher RHgC values and lower OC content in our samples, so even though the studies converge

on similar final numbers, we find underlying sediment chemistry that is notably different than predicted.

We find variable RHgC both across sites and with depth (**Supplementary Figure S7**). Similar to another Arctic study [18], substrate composition plays an important role in soil THg content (**Figure 4B and 4E**) and has an even stronger influence on RHgC values (**Figure 4C and 5F)**. We find few samples with very high OC, and variable soil composition could be a simple explanation for the variable RHgC values — particularly in the case of our peat samples. Our sites were dominated by low OC mineral soils and many of the peat samples were found as laminae in silty layers. It is possible that during formation, periodic river floods allowed water to deposit fine mineral sediment into the peat pore spaces. Samples that appear to be peat may have high mineral soil composition, diluting the percentage of OC. Understanding the causes of varying RHgC in Arctic soils, e.g., via micro-analysis to look at mineral and OC-phase associations of Hg, could be a valuable target for future work. In any case, our results highlight that incorporating sedimentological controls on THg contents and RHgC ratios, and their spatial variability, in models will likely improve estimates of THg stored in permafrost.

Point bar and cutbank stocks in both Huslia and Beaver overlap within uncertainty for most depth intervals (**Figure 5**), although in all cases the median values for cutbanks are higher than for point bars and in some cases the difference is statistically significant. For the full sediment column depth, the cutbank and point bar THg stocks are significantly different at both sites (Beaver $p < 0.001$, Huslia $p < 0.001$). These differences could be explained by the difference in elevation and age of the features: cutbanks have had more time to develop topsoil and accumulate peat in addition to fine grained sediments from overbank deposition, while point bars are lower in elevation and consist of coarser sediment in the top few meters.

Migration and Mobility

Abrupt thaw events can rapidly mobilize meters-thick deposits of sediment, potentially releasing the large Hg stores in permafrost. For example, thaw slumps adjacent to a tributary of the Mackenzie River in Canada were shown to elevate suspended particulate Hg contents downstream, but river Hg loads decreased once the particles settled out of the water column [28]. Our results, based on riverbank stocks, reveal the integrated effects of erosion and sedimentation along multiple eroding bends of the Yukon and Koyukuk Rivers. The nearly balanced THg stocks between cutbanks and point bars in our study suggest that most THg eroded from the banks during river migration is redeposited with sediments in aggrading bars (**Figure 6**), similar to the Mackenzie River slump study [28].

In principle, the sediment budget of cutbank erosion and point bar deposition should be balanced along the river if the river channel is maintaining a constant width over time [45]. Any imbalance would lead to widening (if erosion outpaces deposition) or narrowing over time (if deposition exceeds erosion). If we assume the flux of sediment into the river from erosion is balanced by the flux out of the river via deposition, then comparing the THg in sediment on eroding banks and depositing point bars reveals the net THg flux associated with riverbank

erosion. This framework has been applied to organic carbon fluxes along the Koyukuk River near Huslia [43]. With this approach, we find a net release of Hg from the floodplains to the rivers, because the full column stocks on eroding cutbanks have higher THg than aggrading point bars (**Figure 5**).

We can also relax the assumption of equal rates of bank erosion and deposition, and instead base these fluxes on observed local migration rates from satellite imagery [44], as used to calculate the THg fluxes in **Figure 6**. In this case, the apparently more rapid accretion of point bars at Huslia compared to eroding cutbanks leads to a calculated net deposition of THg from the river into sedimentary deposits. In contrast, high rates of cutbank erosion at Beaver (**Figure 6**), lead to a net erosional release of THg to the river. This spatial difference — with one site exhibiting apparent net Hg erosion and the other deposition — emerges from different erosion rates, emphasizing the importance of quantifying such rates and their spatial variability for understanding biogeochemical responses in a changing Arctic. While satellite-based migration rates may capture a more accurate picture of recent changes over our study sites than assuming balanced erosion and deposition, satellite observations are inherently limited in their time and length scales. Imbalances in erosion and deposition cannot be sustained indefinitely and may not hold over longer reaches of the Yukon and Koyukuk Rivers.

The fluxes per unit river length associated with bank erosion and deposition that we calculate for Huslia and Beaver are 0.6 and 0.3 kg Hg km yr^{-1}. The Yukon River delivers 4,400 kg Hg yr^{-1} to the Arctic Ocean [19], which would equate to 1.38 kg Hg km yr^{-1} just based on the main stem length of ~3200 km. While we recognize that many tributaries contribute to the Yukon (including the Koyukuk) and there are many other sources of Hg to the river across its watershed, this simple comparison reveals that the magnitude of Hg exchange between bank and bar sediments is significant in the context of Yukon River Hg transport. If exchange fluxes in our study areas (**Figure 6**) are representative of the river as a whole, then our results imply that there could be complete exchange of particulate Hg between the river and floodplain over the length of the river. Warming climate is expected to cause permafrost loss and change upland hydrological dynamics, which in turn may alter the pace of this exchange and potentially allow for erosion to outpace deposition. Given the magnitude of the floodplain exchange fluxes, such changes could lead to significant net Hg mobilization from floodplain deposits.

As we find that significant Hg is being eroded in some areas and deposited in others, understanding the extent of Hg mobilization to rivers and its impacts will depend on local sampling because monitoring at a small number of gauging stations may not capture evolving dynamics of Hg mobilization in a changing climate. For example, in the Rio Bermejo, a tributary of the Paraguay River in north Argentina, water flows through the ~1,200 km channel in 14 days, while sediments take on average ~8,500 years [46]. During transport, sediments undergo ~4.5 erosion-deposition events, each taking ~1900 years [47]. In comparison, the Koyukuk spans ~645 km and the Yukon ~3,200 km [30]. As both of these rivers are experiencing active erosion and deposition, it may take decades or longer for geochemical signals to make it to Pilot Station where most river chemistry observations are made on the Yukon River. Our results thus

highlight the importance of accurately capturing the dynamics of erosion and deposition for understanding Hg transport in Arctic rivers and how they will evolve in a changing climate.

Conclusions:

To ground-truth Arctic Hg stocks and evaluate the role of river erosion and deposition in determining particulate Hg fluxes, we conducted two field campaigns along the Koyukuk and Yukon Rivers near the villages of Huslia and Beaver, Alaska, in June and September 2022. We report a median THg $49^{+13}/_{-21}$ ng Hg g soil^{-1} (15th and 85th percentile) (n=195) and a median RHgC of $5.4^{+2}/_{-2.4}$ µg Hg g C^{-1} (n = 186) for sediment samples collected in Huslia and a median THg of $39^{+16}/_{-18}$ ng Hg g soil^{-1} (n = 218) and a median RHgC of $4.2^{+2.4}/_{-2.9}$ µg Hg g C^{-1} (n = 209) for Beaver. We find that THg content was generally higher in sediment with finer grains than coarser grains. Using collected samples and bank stratigraphy characterized in the field, we calculated Hg stocks for 29 banks and 22 bars. Median stock calculations for Huslia and Beaver were generally within the range expected for our study sites based on the Pan-Arctic THg models [15].

Following the framework that the rivers are maintaining constant width, our significantly larger THg stocks on eroding cutbanks in comparison to aggrading point bars imply net release of THg via erosion at both sites. However, satellite-derived migration rates suggest that the rivers are not maintaining constant channel width. We observe faster rates of deposition in Huslia, yielding net THg deposition, and faster rates of erosion in Beaver, suggesting net THg release. Since the magnitude of calculated fluxes are significant at the scale of the YRB, our findings suggest that accounting for river migration rates is critical for assessing changes to Hg transport in Arctic rivers.

Acknowledgement: This work was supported by the National Science Foundation (Grant numbers: #2127442, #2127444, and #2127445), the Geological Society of America, and the Resnick Sustainability Institute at Caltech. We thank the Beaver Village Council and the Huslia Tribal Council for their invaluable support and the opportunity to work on their lands. We also thank our boat drivers and bear guards for guiding us: Alvin Attla, Darin Dayton, Shawn Huffman, Kody Vanderpool, Richard Williams, and Clinton Wiehl. And thank you to Rain Blankenship for processing sediment samples and to Justin Nghiem and Hannah Dion-Kirschner for assistance in the field.

References

[1] Rantanen M, Karpechko AYu, Lipponen A, Nordling K, Hyvärinen O, Ruosteenoja K, et al. The Arctic has warmed nearly four times faster than the globe since 1979. Commun Earth Environ 2022;3:168. https://doi.org/10.1038/s43247-022-00498-3.

[2] van Everdingen RO. Multi-Language Glossary of Permafrost and Related Ground-Ice Terms 2005.

[3] Osterkamp TE, Romanovsky VE. Evidence for warming and thawing of discontinuous permafrost in Alaska. Permafr Periglac Process 1999;10:17–37. https://doi.org/10.1002/(SICI)1099-1530(199901/03)10:1<17::AID-PPP303>3.0.CO;2-4.

[4] Koven CD, Riley WJ, Stern A. Analysis of Permafrost Thermal Dynamics and Response to Climate Change in the CMIP5 Earth System Models. J Clim 2013;26:1877–900. https://doi.org/10.1175/JCLI-D-12-00228.1.

[5] McGuire AD, Lawrence DM, Koven C, Clein JS, Burke E, Chen G, et al. Dependence of the evolution of carbon dynamics in the northern permafrost region on the trajectory of climate change. Proc Natl Acad Sci 2018;115:3882–7. https://doi.org/10.1073/pnas.1719903115.

[6] Chadburn SE, Burke EJ, Cox PM, Friedlingstein P, Hugelius G, Westermann S. An observation-based constraint on permafrost loss as a function of global warming. Nat Clim Change 2017;7:340–4. https://doi.org/10.1038/nclimate3262.

[7] Ramage J, Jungsberg L, Wang S, Westermann S, Lantuit H, Heleniak T. Population living on permafrost in the Arctic. Popul Environ 2021;43:22–38. https://doi.org/10.1007/s11111-020-00370-6.

[8] Arctic Monitoring and Assessment Programme. Arctic Climate Change Update 2021:Key Trends and Impacts. Summary for Policy-makers. Tromsø, Norway: Arctic Council; 2021.

[9] Bronen R. Climate-Induced Displacement of Alaska Native Communities 2013.

[10] Berkes F, Jolly D. Adapting to Climate Change: Social-Ecological Resilience in a Canadian Western Arctic Community. Conserv Ecol 2001;5:art18. https://doi.org/10.5751/ES-00342-050218.

[11] Wesche SD, Chan HM. Adapting to the Impacts of Climate Change on Food Security among Inuit in the Western Canadian Arctic. EcoHealth 2010;7:361–73. https://doi.org/10.1007/s10393-010-0344-8.

[12] Miner KR, D'Andrilli J, Mackelprang R, Edwards A, Malaska MJ, Waldrop MP, et al. Emergent biogeochemical risks from Arctic permafrost degradation. Nat Clim Change 2021;11:809–19. https://doi.org/10.1038/s41558-021-01162-y.

[13] Schaefer K, Elshorbany Y, Jafarov E, Schuster PF, Striegl RG, Wickland KP, et al. Potential impacts of mercury released from thawing permafrost. Nat Commun 2020;11:4650. https://doi.org/10.1038/s41467-020-18398-5.

[14] Durnford D, Dastoor A, Figueras-Nieto D, Ryjkov A. Long range transport of mercury to the Arctic and across Canada. Atmospheric Chem Phys 2010;10:6063–86. https://doi.org/10.5194/acp-10-6063-2010.

[15] Schuster PF, Schaefer KM, Aiken GR, Antweiler RC, Dewild JF, Gryziec JD, et al. Permafrost Stores a Globally Significant Amount of Mercury. Geophys Res Lett 2018;45:1463–71. https://doi.org/10.1002/2017GL075571.

[16] Olson C, Jiskra M, Biester H, Chow J, Obrist D. Mercury in Active-Layer Tundra Soils of Alaska: Concentrations, Pools, Origins, and Spatial Distribution. Glob Biogeochem Cycles 2018;32:1058–73. https://doi.org/10.1029/2017GB005840.

[17] Lim AG, Jiskra M, Sonke JE, Loiko SV, Kosykh N, Pokrovsky OS. A revised pan-Arctic permafrost soil Hg pool based on Western Siberian peat Hg and carbon observations. Biogeosciences 2020;17:3083–97. https://doi.org/10.5194/bg-17-3083-2020.

[18] Rutkowski C, Lenz J, Lang A, Wolter J, Mothes S, Reemtsma T, et al. Mercury in Sediment Core Samples From Deep Siberian Ice-Rich Permafrost. Front Earth Sci 2021;9:718153. https://doi.org/10.3389/feart.2021.718153.

[19] Schuster PF, Striegl RG, Aiken GR, Krabbenhoft DP, Dewild JF, Butler K, et al. Mercury Export from the Yukon River Basin and Potential Response to a Changing Climate. Environ Sci Technol 2011;45:9262–7. https://doi.org/10.1021/es202068b.

[20] López-Berenguer G, Peñalver J, Martínez-López E. A critical review about neurotoxic effects in marine mammals of mercury and other trace elements. Chemosphere 2020;246:125688. https://doi.org/10.1016/j.chemosphere.2019.125688.
[21] Chang LW. Neurotoxic effects of mercury—A review. Environ Res 1977;14:329–73. https://doi.org/10.1016/0013-9351(77)90044-5.
[22] Campbell LM, Norstrom RJ, Hobson KA, Muir DCG, Backus S, Fisk AT. Mercury and other trace elements in a pelagic Arctic marine food web (Northwater Polynya, Baffin Bay). Sci Total Environ 2005;351–352:247–63. https://doi.org/10.1016/j.scitotenv.2005.02.043.
[23] Morel FMM, Kraepiel AML, Amyot M. THE CHEMICAL CYCLE AND BIOACCUMULATION OF MERCURY. Annu Rev Ecol Syst 1998;29:543–66. https://doi.org/10.1146/annurev.ecolsys.29.1.543.
[24] Kozak N, Ahonen SA, Keva O, Østbye K, Taipale SJ, Hayden B, et al. Environmental and biological factors are joint drivers of mercury biomagnification in subarctic lake food webs along a climate and productivity gradient. Sci Total Environ 2021;779:146261. https://doi.org/10.1016/j.scitotenv.2021.146261.
[25] Arctic Monitoring and Assessment Programme. 2021 AMAP Mercury Assessment. Summary for Policy-makers. Tromsø, Norway: Arctic Council; 2021.
[26] Basu N, Abass K, Dietz R, Krümmel E, Rautio A, Weihe P. The impact of mercury contamination on human health in the Arctic: A state of the science review. Sci Total Environ 2022;831:154793. https://doi.org/10.1016/j.scitotenv.2022.154793.
[27] Osterwalder S, Bishop K, Alewell C, Fritsche J, Laudon H, Åkerblom S, et al. Mercury evasion from a boreal peatland shortens the timeline for recovery from legacy pollution. Sci Rep 2017;7:16022. https://doi.org/10.1038/s41598-017-16141-7.
[28] St. Pierre KA, Zolkos S, Shakil S, Tank SE, St. Louis VL, Kokelj SV. Unprecedented Increases in Total and Methyl Mercury Concentrations Downstream of Retrogressive Thaw Slumps in the Western Canadian Arctic. Environ Sci Technol 2018;52:14099–109. https://doi.org/10.1021/acs.est.8b05348.
[29] Zolkos S, Krabbenhoft DP, Suslova A, Tank SE, McClelland JW, Spencer RGM, et al. Mercury Export from Arctic Great Rivers. Environ Sci Technol 2020;54:4140–8. https://doi.org/10.1021/acs.est.9b07145.
[30] Brabets TP, Wang B, Meade RH. Environmental and hydrologic overview of the Yukon River basin, Alaska and Canada. 2000. https://doi.org/10.3133/wri994204.
[31] UAF, USACE. Statewide Threat Assessment: Identification of Threats from Erosion, Flooding, and Thawing Permafrost in Remote Alaska Communities. Denali Commission; 2019.
[32] U.S. Army Corps of Engineers. Alaska Baseline Erosion Assessment. Almendorf Air Force Base, Alaska: 2009.
[33] Rowland JC, Schwenk JP, Shelef E, Muss J, Ahrens D, Stauffer S, et al. Scale-Dependent Influence of Permafrost on Riverbank Erosion Rates. J Geophys Res Earth Surf 2023;128:e2023JF007101. https://doi.org/10.1029/2023JF007101.
[34] Yukon River-Inter-Tribal Watershed Council. YRITWC's IGAP Map 2022.
[35] Douglas M, Blankenship R, Chadwick A, Dunne K, Fischer W, Geyman E, et al. Geomorphic mapping and permafrost occurrence on the Koyukuk River floodplain near Huslia, Alaska 2023. https://doi.org/10.15485/2204419.
[36] Pastick NJ. Probabilistic estimates of the distribution of near-surface permafrost in Alaska 2015. https://doi.org/10.5066/F7C53HX6.
[37] Maxar Technologies. Google Earth n.d.
[38] Earthstar Geographics LLC SIO. Bing Maps n.d.
[39] USGS-Mercury Research Laboratory. Analysis of Total Mercury in Solid Samples by Atomic Adsorption following Direct Combustion with the Nippon MA-2 Mercury Analyzer 2006.
[40] Smith MI, Blankenship R, Douglas MM, Dunne KBJ, Fischer WW, Geyman EC, et al. Mercury content in floodplain sediments from the Yukon River Basin, Alaska, 2022 2024.

https://doi.org/doi:10.18739/A2FX74076.
[41] Ke Y, Blankenship R, Douglas M, Dunne K, Geyman E, Lamb M, et al. Organic carbon content in floodplain sediments from the Yukon River Basin, Alaska 2024. https://doi.org/10.18739/A22R3NZ79.
[42] Miall AD. The Geology of Fluvial Deposits. Berlin, Heidelberg: Springer Berlin Heidelberg; 2006. https://doi.org/10.1007/978-3-662-03237-4.
[43] Douglas MM, Li GK, Fischer WW, Rowland JC, Kemeny PC, West AJ, et al. Organic carbon burial by river meandering partially offsets bank erosion carbon fluxes in a discontinuous permafrost floodplain. Earth Surf Dyn 2022;10:421–35. https://doi.org/10.5194/esurf-10-421-2022.
[44] Geyman E, Avouac J-P, Douglas M, Dunne K, Ke Y, Magyar J, et al. Quantifying river migration rates in the Yukon River Watershed from optical satellite imagery. Arctic Data Center 2024. https://doi.org/urn:uuid:eb84f932-a49a-41b2-a619-5741a2a508df.
[45] Dietrich WE, Smith JD, Dunne T. Flow and Sediment Transport in a Sand Bedded Meander. J Geol 1979;87:305–15. https://doi.org/10.1086/628419.
[46] Repasch M, Scheingross JS, Hovius N, Lupker M, Wittmann H, Haghipour N, et al. Fluvial organic carbon cycling regulated by sediment transit time and mineral protection. Nat Geosci 2021;14:842–8. https://doi.org/10.1038/s41561-021-00845-7.
[47] Repasch M, Wittmann H, Scheingross JS, Sachse D, Szupiany R, Orfeo O, et al. Sediment Transit Time and Floodplain Storage Dynamics in Alluvial Rivers Revealed by Meteoric ^{10}Be. J Geophys Res Earth Surf 2020;125:e2019JF005419. https://doi.org/10.1029/2019JF005419.
[48] U.S. Environmental Protection Agency. Compilation of Air Pollutant Emission Factors, Volume I Stationary Point and Area Sources. Research Triangle Park, NC 27711: U.S. Environmental Protection Agency; 1995.

Environmental Research Letters

Supporting Information

M. Isabel Smith[1,*], Yutian Ke[2], Emily C. Geyman[2], Jocelyn N. Reahl[2], Madison M. Douglas[2,4], Emily A. Seelen[1], John S. Magyar[2], Kieran B.J. Dunne[2,5], Edda A. Mutter[3], Woodward W. Fischer[2], Michael P. Lamb[2], A. Joshua West[1]

1. Department of Earth Sciences, University of Southern California, Los Angeles, CA 90089, USA
2. Division of Geological and Planetary Sciences, California Institute of Technology, Pasadena, CA 91125, USA
3. Yukon River Inter-Tribal Watershed Council, Anchorage, AK 99501, USA
4. Department of Earth, Atmospheric, and Planetary Sciences, Massachusetts Institute of Technology, Cambridge, MA 02139
5. Delft University of Technology, 2628 CD Delft, Netherlands

*Author to whom any correspondence should be addressed.

Email: smithmi@usc.edu

Table of Contents

Text S1: Field Sampling Procedures

Sample sites were accessed by boat and by walking from riverbanks where possible. Fiberglass polycarbonate or plastic trowels were used for sample collection. When sampling from cutbanks, the face of the bank was cleaned with the trowel before sampling. At point bars, pits were dug with a metal spade, and the pit walls were cleaned with the plastic trowel before sampling. Description of stratigraphic layers and thicknesses were noted before sampling. For geochemical samples, someone wearing nitrile gloves collected samples of each stratigraphic layer while a second person labeled and held open sterile WhirlPaks® plastic bags. Geochemical samples were stored in a cooler on board the boat used for accessing sample sites until samples could be frozen (< -15 °C) at basecamp (<10 hours later) until further processing and analysis. After collecting all geochemical samples at a given site, additional samples were taken for bulk density by pressing a metal ring of known volume into the sediment layers. Layers that were too thin to collect bulk density samples were sampled with sediment around them. Bulk density samples were stored in sterile WhirlPaks® bags and left unrefrigerated. In between sampling sites, all equipment was cleaned of sediment using river water and gloved hands.

Text S2: Lab Analysis Procedures

Frozen geochemical samples were freeze dried. Samples were then split following the coning and quartering method [1]. Samples were split on a glass plate with a glass rod to decrease metal contamination. In between each sample, sediment residue left on the glass plate and rod were blown off with compressed air, and surfaces were wiped down with 70% ethanol. After splitting, samples were ground in an agate mortar and pestle and stored in combusted exetainers or sterile WhirlPak bags. The mortar and pestle were cleaned with compressed air and wiped with 70% ethanol between samples. Samples were prepared for analysis on a direct mercury analyzer by weighing ground samples into ceramic boats using teflon coated spatulas. Ceramic boats were loaded into metal trays and analyzed for mercury on a MA-3000. The MA-3000 was calibrated weekly with standards made from diluting a 1000 mg/L Hg Standard Solution (FUJIFILM Wako Pure Chemical Corporation) with a 100 mg/L L-Cysteine and 0.2% nitric acid solution. In between samples, teflon coated spatulas were cleaned with 70% ethanol. Ceramic boats were cleaned between samples by dumping out combusted sediment, sonicating for 30 minutes, drying, and combusting at 450 ℃ for 4 hours.

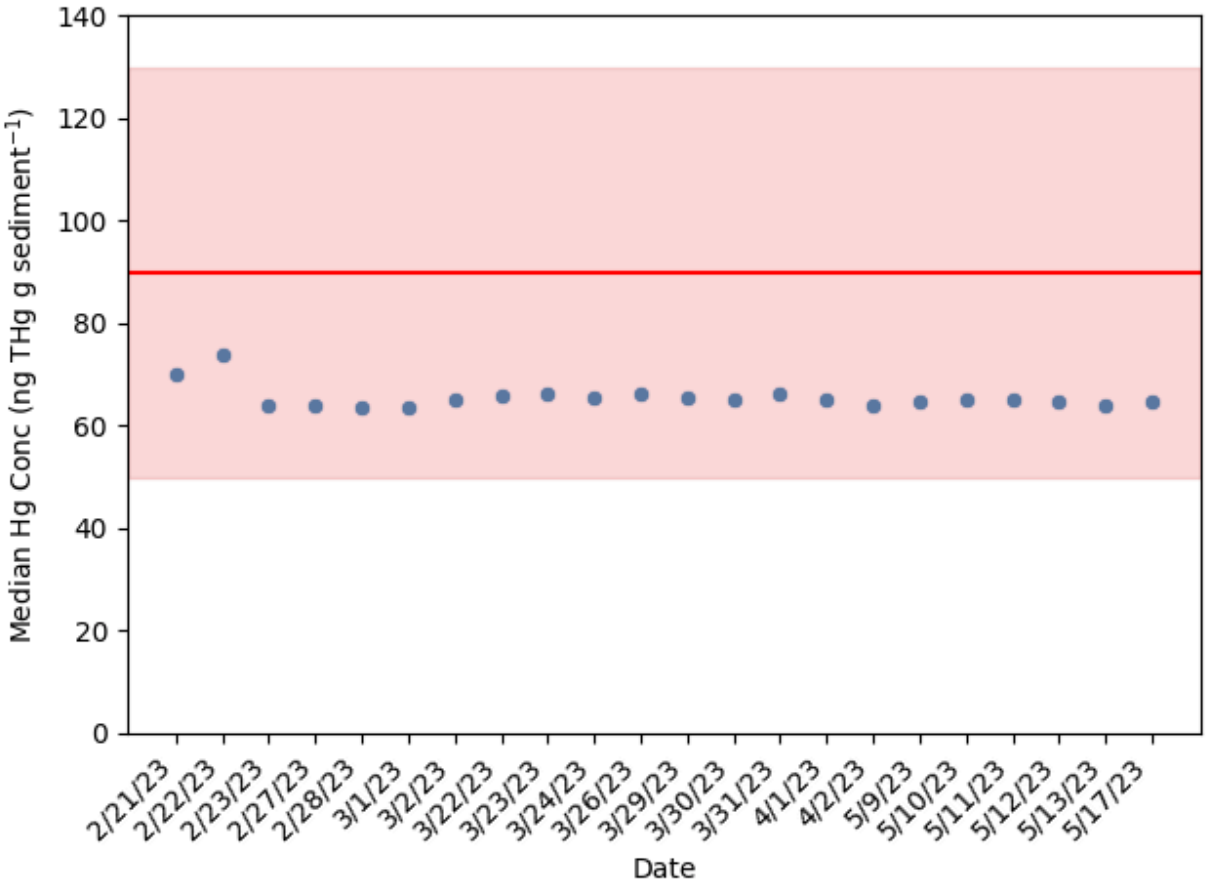

Figure S1: Certified Reference Material (CRM) recoveries. The red line shows the best estimate of the certified value and the red shaded region shows the certified range. The blue dots represent average Hg measurements (n=89) of the CRM on all the 22 dates of analytical analysis. The average measured value was 65 ± 3 ppb with a RSD % = 4. The CRM MESS-4 from National Research Council Canada was used. We used a 6-point calibration curve with the approximate concentrations: 0, 5, 3, 7.5, 25, 60 ng Hg. A blank was used as the 0 ng standard.

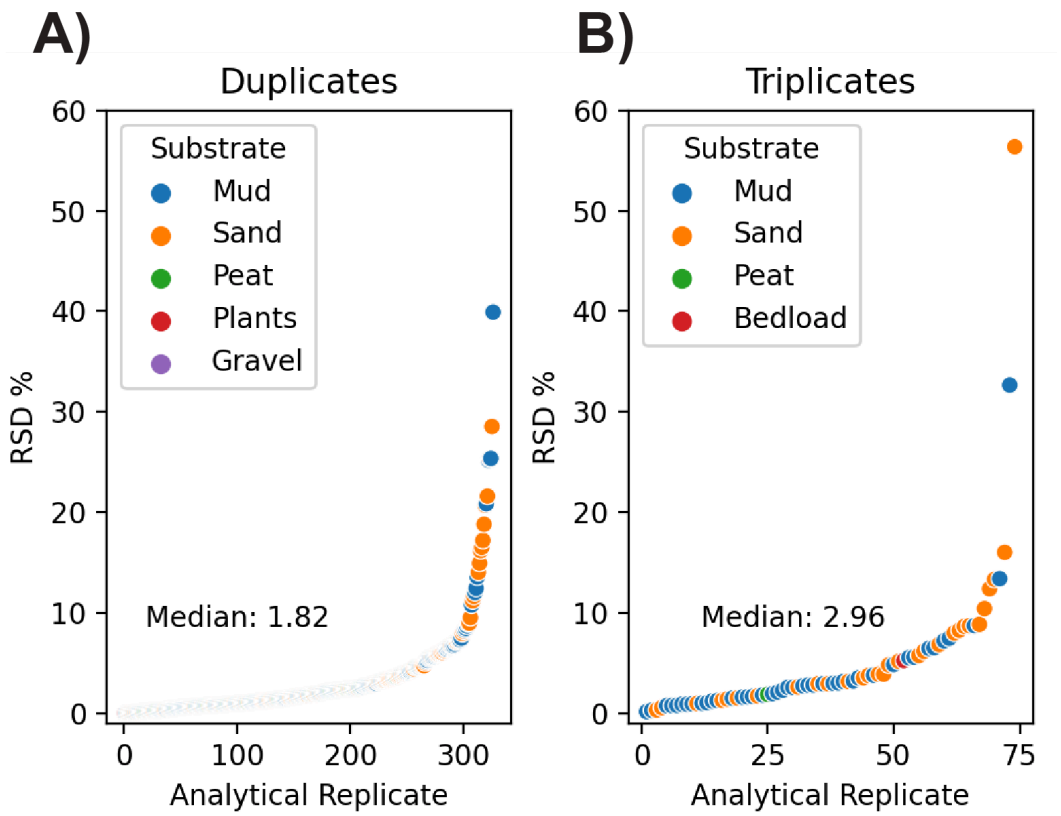

Figure S3: Graphs of analytical (A) duplicates and (B) triplicates. Coloring of dots represents substrate class. Relative Standard Deviation Percent (RSD) for sample duplicates and triplicates (400 out of 413 samples shown). All samples were run in at least duplicate and every set of 10 samples had at least one triplicate (17.91% of samples). RSD ranged from 0.01% to 39.91% with a median value of 2.03% (1.82% for duplicates and 2.96% for triplicates). Samples run more than 3 times had outliers removed using a modified Z-Score approach. Any replicates with Z-Scores greater than ± 3.5 were removed.

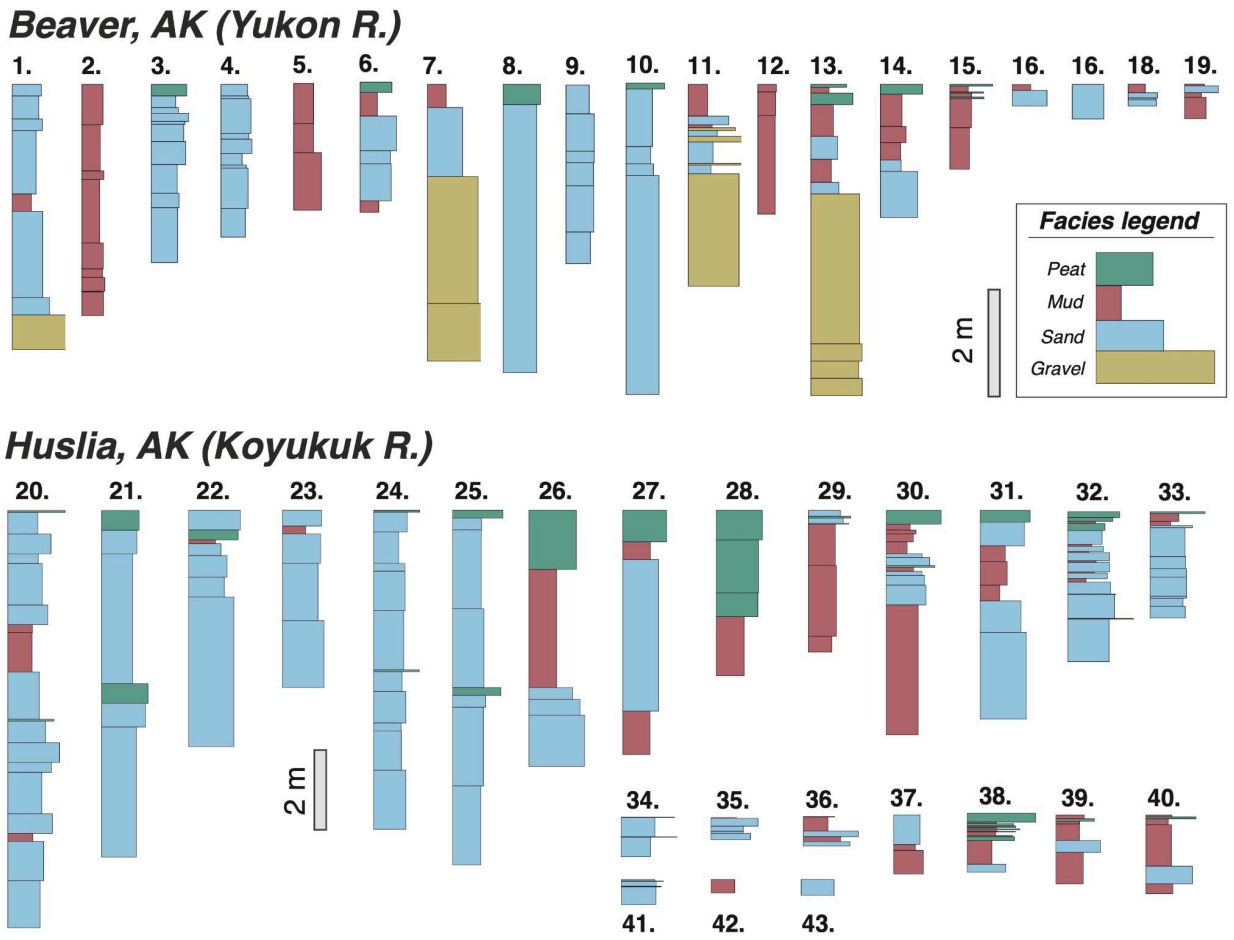

Stratigraphic Column Legend

1. BF22A_B05	11. BS22A_B08	21. HF22B_B10	31. HF22A_B06	41. HS22A_B02
2. BF22B_B01	12. BS22B_B01	22. HF22B_B01	32. HS22B_B02	42. HS22A_B03
3. BF22B_B02	13. BS22B_B12	23. HF22B_B02	33. HS22B_B04	43. HS22A_B20
4. BF22B_B03	14. BS22B_B14	24. HF22B_B11	34. HF22B_B13	
5. BS22A_B02	15. BS22B_B16	25. HF22B_B12	35. HS22A_B01	
6. BS22B_B11	16. BS22A_B01	26. HF22B_B04	36. HS22A_FP01	
7. BF22B_B06b	17. BS22A_B03	27. HF22B_B05	37. HS22B_B09	
8. BF22B_B08	18. BS22A_B06	28. HF22B_B06	38. HF22B_B07	
9. BF22B_B04	19. BS22A_B05	29. HF22B_B08	39. HS22B_B01	
10. BF22B_B06	20. HF22B_B09	30. HF22A_B05	40. HS22B_B01b	

Figure S3: Visual representation of best characterized stratigraphic columns.

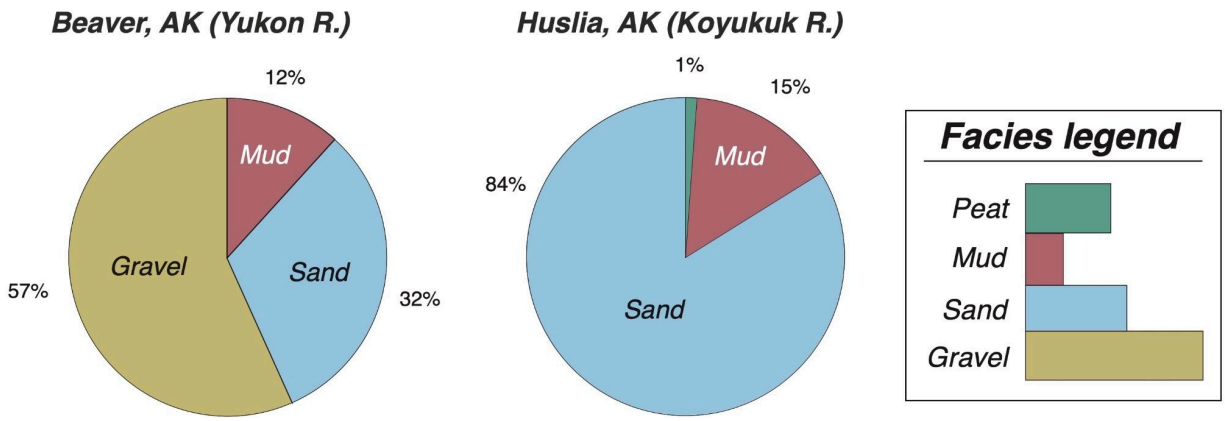

Figure S4: Distribution of alluvial facies for all stratigraphic beds observed below 3 m from the modern floodplain surface.

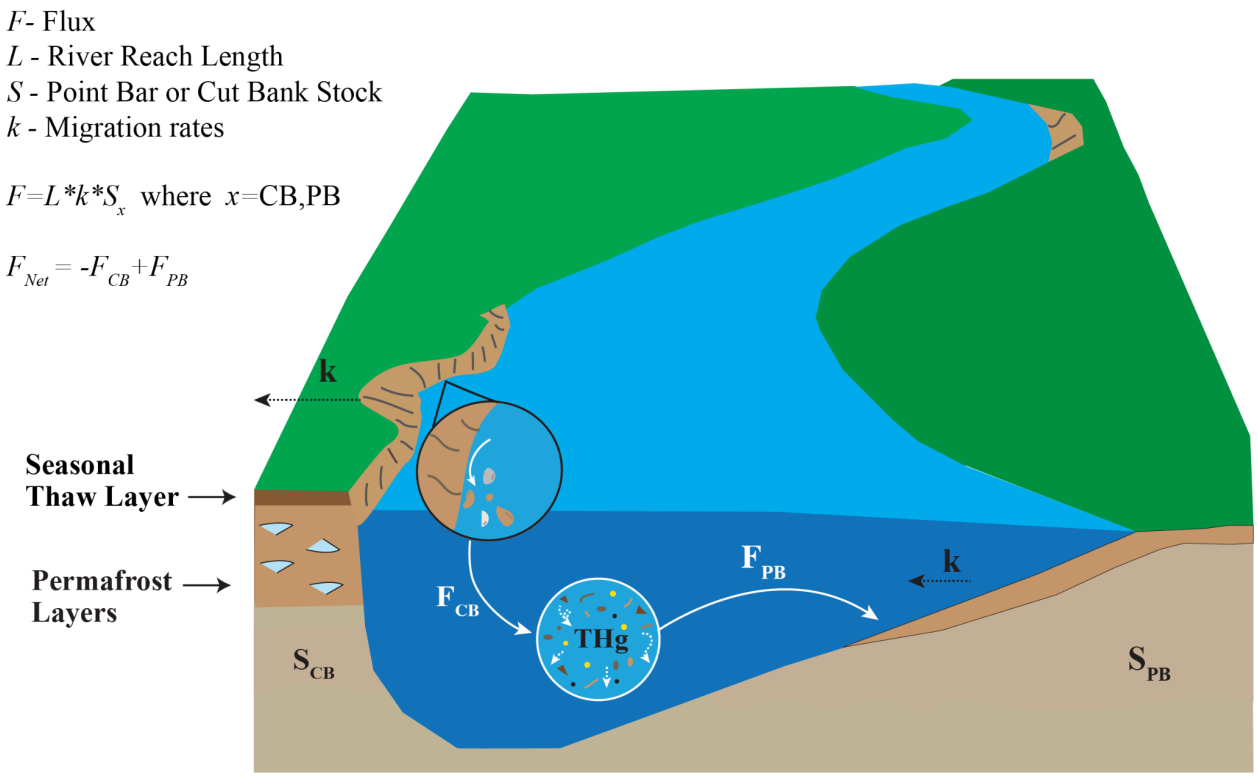

Figure S5: One-dimensional box model representative of a single-threaded meandering river used to study particulate THg fluxes into and out of the river.

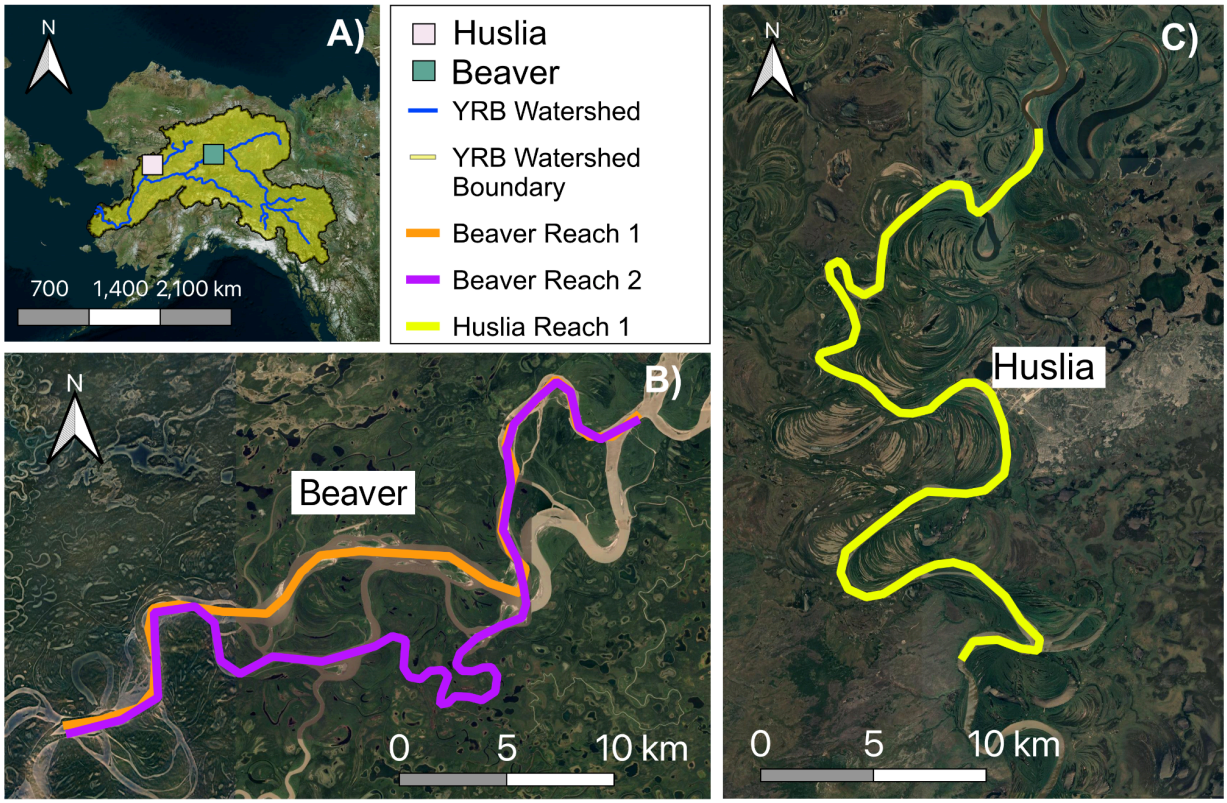

Figure S6: River reach length was determined by tracing satellite imagery of our **A)** study areas on QGIS. Ellipsoidal measuring scales were used. Since **B)** Beaver has two braids, both were traced (Yukon River: purple line ~55 km, orange line ~44 km), but stocks and fluxes used the longer reach because it was more similar to the river reach we measure near **C)** Huslia on the Koyukuk River (yellow line ~58 km).

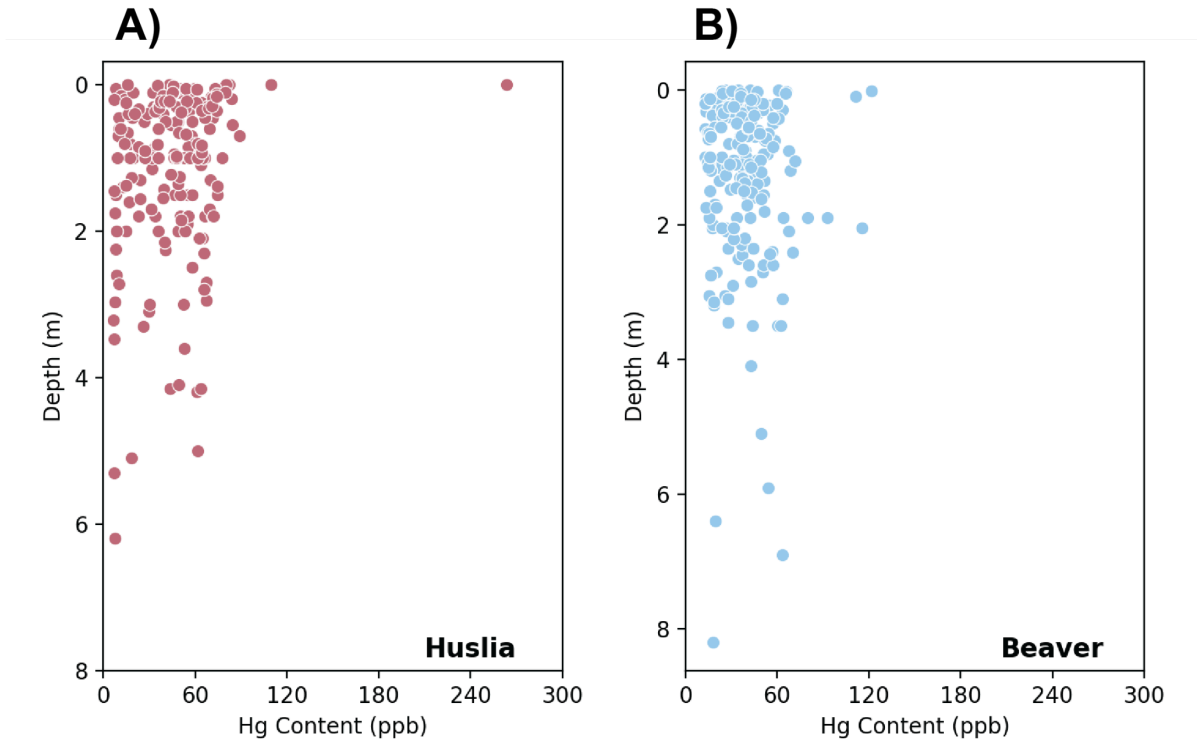

Figure S7: THg depth comparison. Data can be found in **Supplemental Dataset 1**.

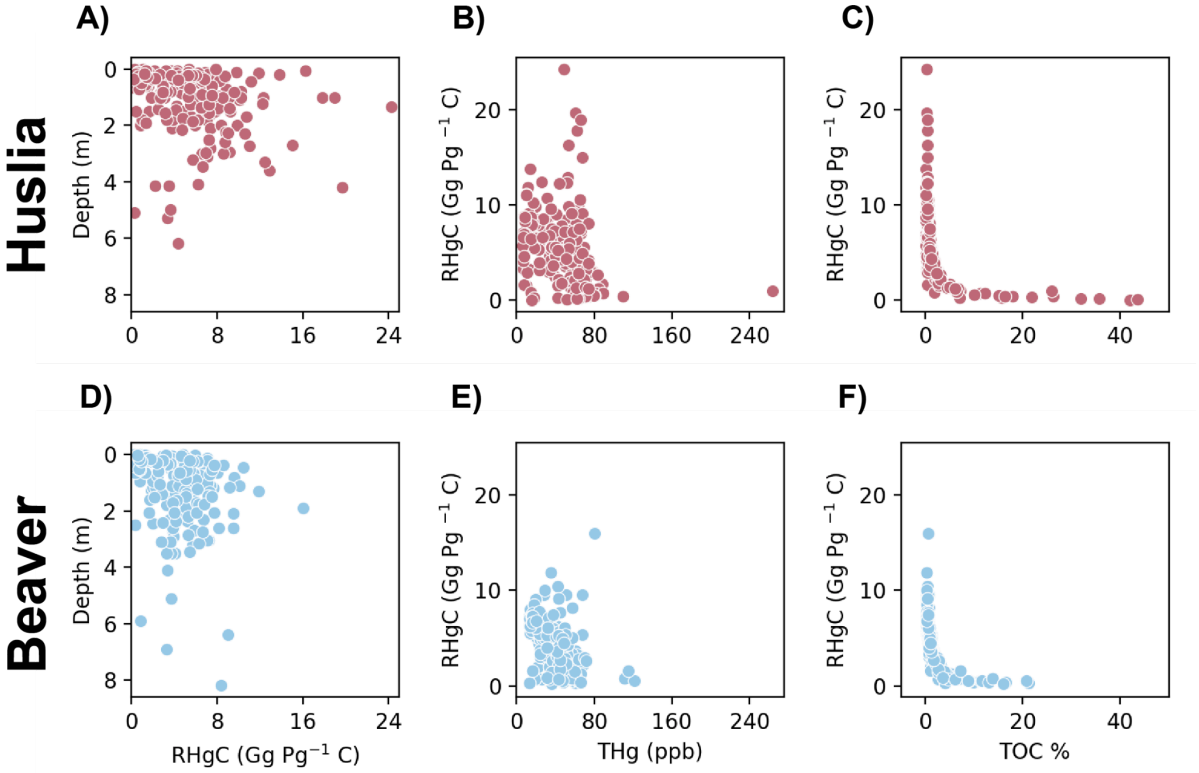

Figure S8: RHgC compared to depth (A,D), THg content (B/E), and (C,F) TOC % in **Supplemental Dataset 1**.

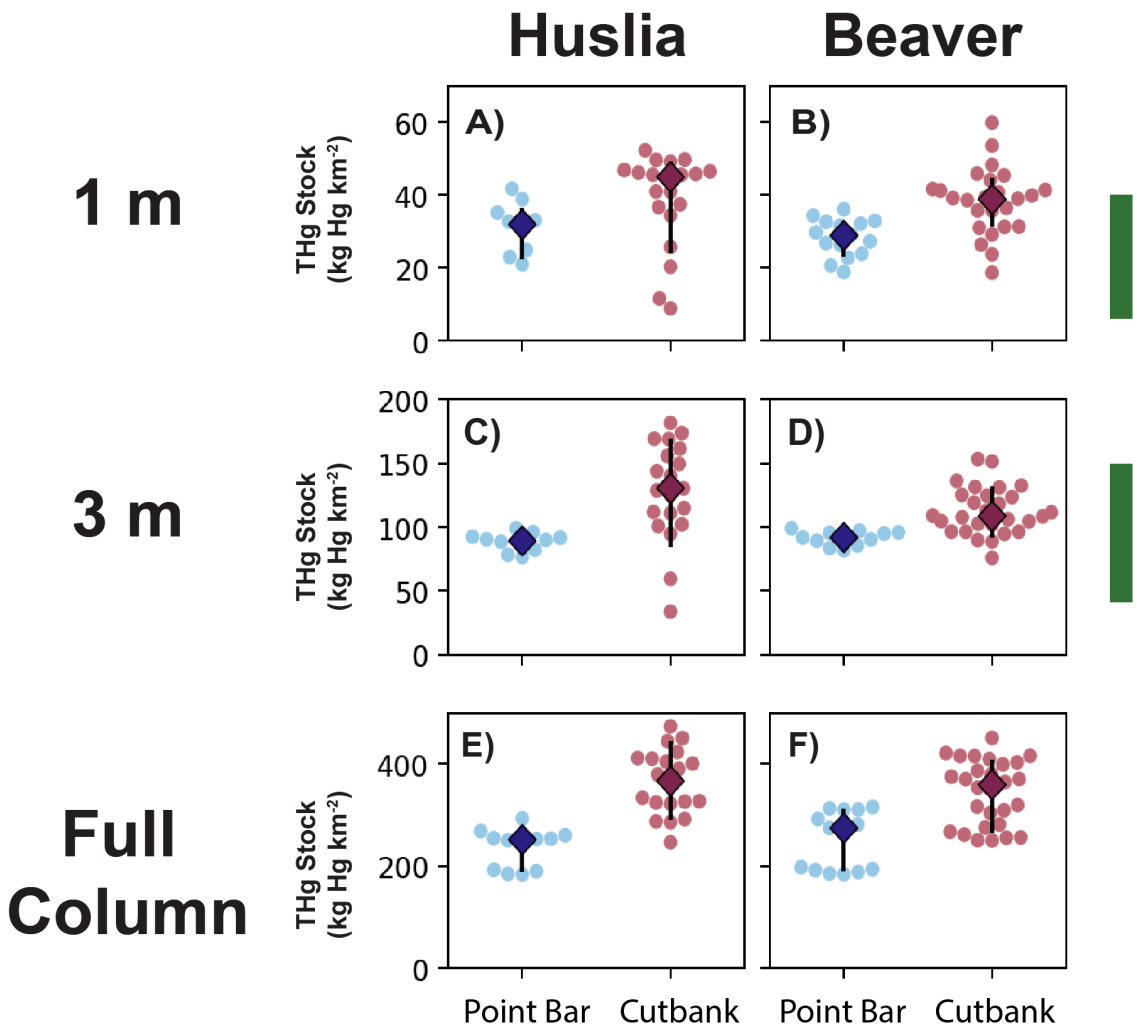

Figure S9: Cutbank and point bar stocks (Huslia: 19 cutbanks and 13 bars; Beaver: 24 cutbanks and 16 bars) calculated for 1 m, 3m, and full bank column using data that included samples with higher percentage of unsampled layers (>30%, **Supplemental, Table S1**). Stock calculations did not include frozen banks denoted by FR (**Supplement**,**Table S1).** Median cutbank stocks changed very little from **Figure 5**. Cutbank stocks with outliers at Huslia were 45 $^{+4}/_{-21}$, 130$^{+39}/_{-46}$, and 367$^{+80}/_{-76}$ kg Hg km sediment^{-2}, over 1 m, 3 m, and total depths, respectively. Equivalent point bar THg stocks at Huslia were 33$^{+4}/_{-11}$, 89$^{+5}/_{-10,}$ and 252$^{+12}/_{-64}$ kg Hg km sediment^{-2}. At Beaver, cutbank stocks were 39$^{+6}/_{-8}$, 109$^{+23}/_{-17}$, and 359$^{+49}/_{-95}$ kg Hg km^{-2}, while point bar stocks were 29$^{+4}/_{-6}$, 92$^{+4}/_{-6}$, and 274$^{+37}/_{-85}$ kg Hg km sediment^{-2}.

Tables S1: Beaver and Huslia stocks with bank heights. Metadata can be found in **Supporting Dataset 1**. Highlighted banks represent columns for which >30% of layers in stock calculation were not measured. Missing layers were supplemented with average values from **Table S2, S3**. * stocks calculated using frozen samples instead of the paired thawed sample. Highlighted and (*) samples were not included in stock or flux calculations (**Figure 5, 6**). Inferred stocks were calculated by multiplying the measured height by the Hg density values on **Table S4.** Total bank height was determined by LiDAR and bathymetry data. Measured heights were collected in the field with a tape measure. Inferred heights were total height minus inferred.

Bank ID	THg Stock (mg Hg m^{-2})					Bank/Bar Height (m)		
	1 m	3 m	Measured	Inferred	Total Bank	Total	Measured	Inferred
BF22A_B01 (Pit 1)	22.81	85.60	7.11	177.26	184.36	7.30	0.50	6.80
BF22A_B01 (Pit 2)	23.95	86.74	8.25	177.26	185.50	7.30	0.50	6.80
BF22A_B01 (Pit 3)	36.10	98.90	20.40	177.26	197.66	7.30	0.50	6.80
BF22A_B01 (Pit 4)	31.61	94.41	15.91	177.26	193.17	7.30	0.50	6.80
BF22A_B01 (Pit 5)	32.15	94.95	16.45	177.26	193.71	7.30	0.50	6.80
BF22A_B01 (Pit 6)	26.87	89.66	11.17	177.26	188.42	7.30	0.50	6.80
BF22A_B05	31.07	96.35	143.73	123.56	267.26	9.34	4.6	4.74
BF22A_B11	44.22	131.20	214.62	201.32	415.86	13.52	5.8	7.72
BF22B_B01	23.79	111.39	276.20	93.99	370.18	11.80	8.2	3.60
*BF22B_B01FR	23.79	123.52	291.84	93.99	385.82	11.80	8.2	3.60
BF22B_B02	44.17	138.52	135.06	169.44	304.51	9.39	2.89	6.50
BF22B_B03	31.37	106.09	95.13	160.67	255.77	8.81	2.65	6.16
BF22B_B04	37.19	132.46	135.93	173.63	309.51	9.76	3.1	6.66
*BF22B_B04FR	39.00	104.72	108.17	173.63	281.77	9.76	3.1	6.66
BF22B_B06	40.79	88.55	129.68	252.78	382.46	14.49	4.8	9.69
*BF22B_B06FR	41.27	102.47	150.71	252.78	403.49	14.49	4.8	9.69
BF22B_B07	39.90	125.23	219.67	196.11	415.71	13.52	6	7.52
BF22B_B08	41.68	136.16	230.64	190.60	421.24	12.31	5	7.31
*BF22B_B08FR	45.89	153.34	260.79	190.60	451.39	12.31	5	7.31
BF22B_B09 (Pit 1)	20.70	83.49	11.28	263.34	274.61	10.80	0.7	10.10

BF22B_B09 (Pit 2)	29.04	91.83	11.77	269.86	281.62	10.80	0.45	10.35
BF22B_B09 (Pit 3)	32.67	95.47	15.40	269.86	285.26	10.80	0.45	10.35
BF22B_B09 (Pit 4)	18.88	81.68	16.69	257.34	274.03	10.80	0.93	9.87
BF22B_B11 (Pit 1)	29.79	92.58	18.80	294.22	313.01	11.93	0.65	11.28
BF22B_B11 (Pit 2)	34.39	97.19	12.41	303.34	315.76	11.93	0.3	11.63
BS22A_B01	27.34	90.13	7.56	284.67	292.23	11.29	0.37	10.92
BS22A_B02	35.76	108.31	83.20	167.43	250.62	8.62	2.2	6.42
*BS22A_B02FR	35.76	107.62	83.20	167.43	249.92	8.62	2.2	6.42
BS22A_B03	26.31	89.10	13.75	178.08	191.83	7.43	0.6	6.83
BS22A_B05	32.93	95.73	19.43	291.26	310.69	11.74	0.57	11.17
BS22A_B06	28.86	91.65	9.39	301.66	311.05	11.95	0.38	11.57
BS22B_B01	34.48	119.01	101.21	315.07	416.18	14.51	2.43	12.08
*BS22B_B01FR	29.17	112.66	94.77	315.07	409.84	14.51	2.43	12.08
BS22B_B02	18.70	74.28	91.52	228.02	319.55	12.29	3.55	8.74
BS22B_B03	38.60	89.67	81.87	293.44	375.26	14.00	2.75	11.25
BS22B_B04	26.45	94.74	75.92	294.57	370.46	13.70	2.4	11.30
BS22B_B05	32.68	75.79	78.34	197.22	275.55	10.66	3.1	7.56
BS22B_B07	59.87	151.31	191.46	195.58	387.02	11.30	3.80	7.50
BS22B_B08	36.51	104.50	85.66	176.09	261.75	9.15	2.4	6.75
BS22B_B10 Core 1	41.43	108.87	66.81	298.04	364.83	13.09	1.66	11.43
BS22B_B10 Core 2	39.16	101.95	37.59	316.56	354.14	13.09	0.95	12.14
BS22B_B11	48.31	130.87	123.34	257.29	380.62	12.63	2.76	9.87
BS22B_B12	39.30	96.27	132.82	266.24	399.02	14.61	4.4	10.21
BS22B_B16	45.40	118.10	70.07	186.33	256.39	8.62	1.47	7.15
BS22B_B18	31.31	96.31	60.22	256.31	316.51	11.68	1.85	9.83
BS22B_B19	53.58	124.64	178.51	172.87	351.36	11.68	5.05	6.63
HF22A_B01 (Pit 1)	41.74	98.85	30.32	162.33	192.66	6.83	0.6	6.23
HF22A_B01 (Pit 2)	33.10	90.20	18.82	164.94	183.76	6.83	0.5	6.33
HF22A_B01 (Pit 3)	34.41	91.51	17.28	167.55	184.83	6.83	0.4	6.43

HF22A_B02	11.59	59.34	16.51	305.76	322.28	13.23	1.5	11.73
HF22A_B03 (Pit 1)	21.02	78.12	12.46	237.98	250.44	9.83	0.7	9.13
HF22A_B03 (Pit 2)	31.21	88.31	21.22	239.28	260.50	9.83	0.65	9.18
HF22A_B03 (Pit 3)	31.25	88.36	29.83	263.54	293.36	9.83	0.95	8.88
HF22A_B04 (Pit 1)	19.38	76.48	5.10	243.20	248.30	9.83	0.5	9.33
HF22A_B04 (Pit 2)	23.04	80.14	21.61	231.46	253.08	9.83	0.95	8.88
HF22A_B04 (Pit 3)	38.88	95.98	33.17	235.37	268.54	9.83	0.8	9.03
HF22A_B05	45.59	155.81	333.53	126.66	460.19	10.56	5.7	4.86
*HF22A_B05FR	45.57	128.61	285.08	126.66	411.74	10.56	5.7	4.86
HF22A_B06	36.76	173.72	290.15	160.81	450.95	11.47	5.3	6.17
HF22B_B01	49.60	168.87	331.37	142.55	473.92	11.47	6	5.47
HF22B_B02	44.97	111.73	158.56	168.76	327.32	10.97	4.5	6.47
HF22B_B04	40.99	100.64	207.66	118.98	326.64	11.06	6.5	4.56
*HF22B_B04FR	41.02	114.85	260.83	118.98	379.82	11.06	6.5	4.56
HF22B_B06	34.44	101.90	190.22	176.58	366.80	10.97	4.2	6.77
HF22B_B07	46.16	169.10	226.17	184.40	410.58	10.97	3.9	7.07
HF22B_B08	49.15	149.40	171.75	218.87	390.62	10.97	3.6	7.37
HF22B_B09	49.64	140.08	255.00	168.42	423.42	10.97	5.3	5.67
HF22B_B10	52.30	181.61	273.38	171.37	444.74	10.97	4.4	6.57
HF22B_B11	45.80	143.81	195.43	205.51	400.93	10.97	4.05	6.92
HF22B_B12	46.50	161.43	236.07	168.76	404.83	10.97	4.5	6.47
HF22B_B13	37.51	94.61	23.23	310.91	334.14	10.97	0.5	10.47
HS22A_B01	24.95	82.05	13.53	240.18	253.71	9.81	0.6	9.21
HS22A_B03	35.21	92.32	16.37	173.60	189.97	7.00	0.34	6.66
HS22A_FP01	32.68	89.78	25.40	229.49	254.89	9.55	0.745	8.80
HS22B_B01	25.75	130.43	70.51	217.19	287.70	10.08	1.75	8.33
*HS22B_B01FR	49.72	130.16	94.47	217.19	311.66	10.08	1.75	8.33
HS22B_B02.1	20.37	51.40	59.62	186.75	246.38	10.97	3.81	7.16
HS22B_B02.2	8.92	33.65	37.10	255.00	292.10	13.21	3.43	9.78
HS22B_B04	38.68	124.97	116.41	169.65	286.06	9.21	2.7	6.51
HS22B_B09	46.88	110.72	67.89	256.67	324.56	11.34	1.5	9.84

Table S2: Table of averages dry density and Hg content used for stock calculations at Beaver. Dry density and Hg content ± standard deviation.

Facies	Average Dry Density (g/mL)	Average THg Content (ppb)	*Hg Density (mg Hg m^{-3})
Sand	(n = 25) 1.06 ± 0.18	(n = 92) 29.61 ± 12.47	31.40 ± 14.25
Mud	(n = 27) 0.92 ± 0.29	(n = 108) 44.64 ± 13.16	40.86 ± 17.59
Peat	(n = 5) 0.48 ± 0.37	(n = 17) 65.51 ± 25.18	31.35 ± 27.23
Gravel	(n = 5) 1.57 ± 0.32	(n = 1) **16.63 ± 0.67	26.08 ± 5.38

*Hg density was calculated by multiplying the average dry density and average Hg content of the same facies together from **Supplemental Dataset 1**. Uncertainties on Hg density are 1σ errors from propagation of uncertainties on dry density and Hg content.
Since there was only 1 measurement, uncertainty was assumed to be 4% based off of median CRM RSD % (Figure S1**).

Table S3: Table of averages dry density and Hg content used for stock calculations at Huslia. Dry density and Hg content ± standard deviation of sample.

Facies	Average Dry Density (g/mL)	Average THg Content (ppb)	*THg Density (mg Hg m^{-3})
Sand	(n = 38) 1.25 ± 0.23	(n = 51) 22.79 ± 18.05	28.55 ± 23.20
Mud	(n = 66) 0.95 ± 0.25	(n = 129) 51.51 ± 16.04	49.08 ± 20.11
Peat	(n = 10) 0.27 ± 0.18	(n = 15) 81.79 ± 54.57	21.81 ± 20.62

*Hg density was calculated by multiplying the average dry density and average Hg content of the same facies together **Supplemental Dataset 1**. Uncertainties on Hg density are 1σ errors from propagation of uncertainties on dry density and Hg content.

Table S4: Constants values for flux calculations.

Facies	River Reach Length (m)	THg Density (mg Hg/m^{-3})
Sand (from Huslia)	58000	28.55 ± 23.20
Gravel (from Beaver)	55000	26.08 ± 5.38

Table S5: Table of erosion rates [2], total bank stocks, and calculated fluxes. Fluxes were calculated by multiplying erosion rate, total bank stock, and river reach. Highlighted banks represent columns for which >30% of layers in stock calculation were not measured. Those banks were not used in the Main Text and **Figure 6**.

Bank ID	Erosion Rate (m/yr)	Total Bank THg Stock (mg Hg m^{-2})	River Reach (m)	Flux (kg THg km^{-2})
BF22A_B01 (Pit 1)	0.99	184.36	See Supplemental **Figure S4**	10.09
BF22A_B01 (Pit 2)	0.99	185.50		10.15
BF22A_B01 (Pit 3)	0.99	197.66		10.81
BF22A_B01 (Pit 4)	0.99	193.17		10.57
BF22A_B01 (Pit 5)	0.99	193.71		10.60
BF22A_B01 (Pit 6)	0.99	188.42		10.31
BF22A_B05	1.00	267.26		14.70
BF22A_B11	9.83	415.86		224.90
BF22B_B01	1.42	370.18		28.95
*BF22B_B01FR	1.42	385.82		30.17
BF22B_B02	1.00	304.51		16.72
BF22B_B03	0.93	255.77		13.13
BF22B_B04	0.10	309.51		1.74
*BF22B_B04FR	0.10	281.77		1.58
BF22B_B06	6.18	382.46		129.91
*BF22B_B06FR	6.18	403.49		137.05
BF22B_B07	10.63	415.71		243.11

BF22B_B08	12.03	421.24	**See Supplemental Figure S4**	278.78
*BF22B_B08FR	12.03	451.39		298.73
BF22B_B09 (Pit 1)	1.03	274.61		15.55
BF22B_B09 (Pit 2)	1.03	281.62		15.94
BF22B_B09 (Pit 3)	1.03	285.26		16.15
BF22B_B09 (Pit 4)	1.03	274.03		15.51
BF22B_B11 (Pit 1)	0.34	313.01		5.90
BF22B_B11 (Pit 2)	0.34	315.76		5.95
BS22A_B01	0.52	292.23		8.38
BS22A_B02	0.70	250.62		9.67
*BS22A_B02FR	0.70	249.92		9.65
BS22A_B03	0.92	191.83		9.71
BS22A_B05	0.52	310.69		8.81
BS22A_B06	0.54	311.05		9.19
BS22B_B01	6.04	416.18		138.24
*BS22B_B01FR	6.04	409.84		136.14
BS22B_B02	1.40	319.55		24.63
BS22B_B03	3.25	375.26		67.12
BS22B_B04	1.66	370.46		33.90
BS22B_B05	0.26	275.55		3.91
BS22B_B07	1.27	387.02		26.96
BS22B_B08	1.24	261.75		17.81
BS22B_B10 Core 1	9.23	364.83		185.19
BS22B_B10 Core 2	9.23	354.14		179.76
BS22B_B11	11.28	380.62		236.10
BS22B_B12	2.70	399.02		59.27
BS22B_B16	1.30	256.39		18.33
BS22B_B18	3.47	316.51		60.34

BS22B_B19	3.47	351.36		66.99
HF22A_B01 (Pit 1)	4.53	192.66		50.66
HF22A_B01 (Pit 2)	4.53	183.76		48.32
HF22A_B01 (Pit 3)	4.53	184.83		48.60
HF22A_B02	4.96	322.28		92.78
HF22A_B03 (Pit 1)	6.31	250.44		91.59
HF22A_B03 (Pit 2)	6.31	260.50		95.28
HF22A_B03 (Pit 3)	6.31	293.36		107.29
HF22A_B04 (Pit 1)	7.02	248.30		101.05
HF22A_B04 (Pit 2)	7.02	253.08		102.99
HF22A_B04 (Pit 3)	7.02	268.54		109.28
HF22A_B05	3.70	460.19		98.84
*HF22A_B05FR	3.70	411.74		88.44
HF22A_B06	0.63	450.95	**See Supplemental Figure S4**	16.46
HF22B_B01	6.04	473.92		166.11
HF22B_B02	1.90	327.32		36.03
HF22B_B04	5.66	326.64		107.30
*HF22B_B04FR	5.66	379.82		124.77
HF22B_B06	1.45	366.80		30.74
HF22B_B07	2.51	410.58		59.89
HF22B_B08	3.53	390.62		80.03
HF22B_B09	1.60	423.42		39.28
HF22B_B10	1.59	444.74		41.08
HF22B_B11	1.60	400.93		37.14
HF22B_B12	1.55	404.83		36.35
HF22B_B13	1.85	334.14		35.82
HS22A_B01	7.58	253.71		111.49
HS22A_B03	4.16	189.97		45.79

HS22A_FP01	7.10	254.89	**See Supplemental Figure S4**	104.98
HS22B_B01	6.01	287.70		100.30
*HS22B_B01FR	6.01	311.66		108.65
HS22B_B02.1	5.05	246.38		72.20
HS22B_B02.2	5.05	292.10		85.60
HS22B_B04	1.90	286.06		31.58
HS22B_B09	0.67	324.56		12.54

Table S6: Mercury content for frozen (FR) and thawed (TH) samples from Huslia and Beaver. Additional information on samples can be found in **Supplemental Dataset 1**.
* paired sample

Site	**Sample ID**	**Hg Content (ppb)**
Huslia	*HS22B_B01_S04TH	64.41
Huslia	*HS22B_B01_S05FR	68.00
Huslia	HF22A_B05_S07FR	24.01
Huslia	HF22A_B05_S07TH	70.10
Huslia	HF22A_B05_S11FR	23.22
Huslia	HF22A_B05_S11TH	66.44
Huslia	HF22A_B05_S13FR	78.03
Huslia	HF22A_B05_S13TH	88.07
Huslia	HF22B_B04_S04FR	43.72
Huslia	HF22B_B04_S04TH	63.74
Beaver	BF22B_B01_S06FR2	60.37
Beaver	BF22B_B01_S06FR1	62.42
Beaver	BF22B_B01_S06TH	44.09
Beaver	BF22B_B04_S06FR	27.00
Beaver	BF22B_B04_S06TH	67.67
Beaver	BF22B_B06_S03FR	26.12
Beaver	BF22B_B06_S03TH	15.83
Beaver	BF22B_B06_S04FR	22.45

Beaver	BF22B_B06_S04TH	40.00
Beaver	BF22B_B06_S05FR	27.67
Beaver	BF22B_B06_S05TH	21.69
Beaver	BF22B_B06_S06FR	23.83
Beaver	BF22B_B06_S06TH	13.29
Beaver	BF22B_B08_S04FR	80.09
Beaver	BF22B_B08_S04TH	64.01
Beaver	BF22B_B08_S05FR	39.73
Beaver	BF22B_B08_S05TH	36.88
Beaver	BF22B_B08_S06FR	51.40
Beaver	BF22B_B08_S06TH	57.17
Beaver	BS22B_B01_S06FR	51.83
Beaver	BS22B_B01_S06TH	40.84
Beaver	BS22B_B01_S12FR	47.78
Beaver	BS22B_B01_S12TH	54.25

References

[1] U.S. Environmental Protection Agency. Compilation of Air Pollutant Emission Factors, Volume I Stationary Point and Area Sources. Research Triangle Park, NC 27711: U.S. Environmental Protection Agency; 1995.

[2] Geyman E, Avouac J-P, Douglas M, Dunne K, Ke Y, Magyar J, et al. Quantifying river migration rates in the Yukon River Watershed from optical satellite imagery, Alaska, 2016-2022. 2024. https://doi.org/doi:10.18739/A2WW7719J.